Geoscientific
Model Development

Modeling of streamflow in a 30 km long reach spanning 5 years using OpenFOAM 5.x

Yunxiang Chen, Jie Bao, Yilin Fang, William A. Perkins, Huiying Ren, Xuehang Song, Zhuoran Duan, Zhangshuan Hou, Xiaoliang He, and Timothy D. Scheibe

Pacific Northwest National Laboratory, Richland, WA, USA

Correspondence: Yunxiang Chen (yunxiang.chen@pnnl.gov)

Abstract. Developing accurate and efficient modeling techniques for streamflow at the tens-of-kilometers spatial scale and multi-year temporal scale is critical for evaluating and predicting the impact of climate- and human-induced discharge variations on river hydrodynamics. However, achieving such a goal is challenging because of limited surveys of streambed hydraulic roughness, uncertain boundary condition specifications, and high computational costs. We demonstrate that accurate and efficient three-dimensional (3-D) hydrodynamic modeling of natural rivers at 30 km and 5-year scales is feasible using the following three techniques within OpenFOAM, an open-source computational fluid dynamics platform: (1) generating a distributed hydraulic roughness field for the streambed by integrating water-stage observation data, a rough wall theory, and a local roughness optimization and adjustment strategy; (2) prescribing the boundary condition for the inflow and outflow by integrating precomputed results of a one-dimensional (1-D) hydraulic model with the 3-D model; and (3) reducing computational time using multiple parallel runs constrained by 1-D inflow and outflow boundary conditions. Streamflow modeling for a 30 km long reach in the Columbia River (CR) over 58 months can be achieved in less than 6 d using 1.1 million CPU hours. The mean error between the modeled and the observed water stages for our simulated CR reach ranges from -16 to 9 cm (equivalent to approximately $\pm 7\%$ relative to the average water depth) at seven locations during most of the years between 2011 and 2019. We can reproduce the velocity distribution measured by the acoustic Doppler current profiler (ADCP). The correlation coefficients of the depth-averaged velocity between the model and ADCP measurements are in the range between 0.71 and 0.83 at 75 % of the survey cross sections. With the validated model, we further show that the relative importance of dynamic pressure versus hydrostatic pressure varies with discharge variations and topography heterogeneity. Given the model's high accuracy and computational efficiency, the model framework provides a generic approach to evaluate and predict the impacts of climate- and human-induced discharge variations on river hydrodynamics at tens-of-kilometers and decadal scales.

1 Introduction

As a major element of the water cycle, streamflow varies with upstream discharge, interacts with ambient physical and biological environments, and thus creates a variety of social, economic, and environmental functions (Wampler, 2012; Wohl et al., 2015; Harvey, 2016; Biddanda, 2017; Hiemstra et al., 2020). For instance, the flood control function is largely determined by accurate predictions of the water depth and flow speed that are further controlled by upstream discharge variations and the hydraulic roughness generated by flow–streambed interactions (USACE, 1994; Ferguson, 2019). The water quality management and biodiversity protection functions are strongly affected by the hydrological exchange flows (Harvey, 2016) that are driven by hydrostatic pressure and flow-sediment-induced dynamic pressure (Tonina and Buffington, 2007; Cardenas and Wilson, 2007). As the magnitude, frequency, and peak time of discharge are projected to vary with future climate and anthropogenic conditions (Potter et al., 2004; Veldkamp et al., 2018; Wei et al., 2020; Xu et al., 2021), it is essential to establish a numerical modeling framework that enables evaluating and predicting

the impact of climate- or human-induced discharge variations on streamflow and river functions.

Over the past three decades, computational fluid dynamics (CFD) models at various dimensions have been developed and applied to model streamflow (Bates et al., 2005). By solving the one-dimensional (1-D) Saint-Venant equations, 1-D numerical models have been widely used to predict flood routing (Richards, 1978; Keller and Florsheim, 1993; Carling and Wood, 1994; Hicks and Peacock, 2005), sediment transport (van Niekerk et al., 1992; Correia et al., 1992; Hoey and Ferguson, 1994; Ferguson et al., 2001; Talbot and Lapointe, 2002; Cui et al., 2003), water quality (Richmond et al., 2002), and aquatic habitats (Bovee, 1978; Milhous et al., 1984). A lot of software based on the 1-D models, e.g., HEC-RAS, MIKE-11, ISIS, and InfoWorks, has also been developed and commercialized for practical applications. As the 1-D models provide only cross-sectional averaged velocity and water depth, these models are usually problematic if flow manifests large variations in either the vertical or the cross-sectional direction (Lane and Ferguson, 2005). Due to these reasons, the two-dimensional (2-D) numerical models, which solve the depth-averaged Navier–Stokes equations, have been developed to better capture the cross-sectional variations in flow (Miller, 1994; Bates et al., 1995; Lane and Richards, 1998; Thompson et al., 1998; Cao et al., 2003) and resulted influences on sediment transport (Howard, 1992; Sun et al., 1996; Nagata et al., 2000; Duan et al., 2001; Darby et al., 2002), water quality (Perkins and Richmond, 2007), and aquatic habitats (Leclerc et al., 1995; Crowder and Diplas, 2000). Armed with increasingly powerful personal and high-performance computers, commercial 2-D models such as HEC-RAS and SRH-2D are frequently deployed for flood management in urban and mountain areas. Despite the wide applications of 2-D models, quasi-3-D models are also gaining popularity because of increasing computer capacity and the capability to predict the vertical velocity component. Though quasi-3-D models, e.g., Princeton Ocean Model (Blumberg and Mellor, 1983), Environmental Fluid Dynamics Code-3D (Hamrick, 1992), Delft3D (Lesser et al., 2004), and CH3D (Johnson et al., 1993), have been commonly used for ocean, coastal, and river applications, they are not adequate to model the dynamic pressure.

As the dynamic pressure is a key driver of the flow, momentum, and nutrient exchange between stream water and ambient environments, e.g., meander river planform, complex instream structures, and groundwater, non-hydrostatic or fully 3-D Navier–Stokes models are required in order to reliably predict rivers' environmental and ecological functions under dynamic discharge conditions (Lorke and MacIntyre, 2009; Harvey, 2016; Hester et al., 2017; Chen et al., 2019). The full 3-D simulations were firstly restricted to rivers with rectangular cross sections (Leschziner and Rodi, 1979; Demuren and Rodi, 1986) and then were gradually extended for small-scale natural rivers with meander and roughness (Demuren, 1993; Olsen and Stokseth, 1995; Hod-

skinson, 1996; Hodskinson and Ferguson, 1998). A more realistic application is given by Sinha et al. (1998), whose work resolved the effects of large-scale roughness and multiple islands on streamflow in a 4 km stretch of the Columbia River. Later, more 3-D models were applied to study hydrodynamics in natural streams (Nicholas and Sambrook Smith, 1999; Lane et al., 1999; Booker et al., 2001; Ma et al., 2002; Rodriguez et al., 2004; Huang et al., 2004; Lane and Ferguson, 2005; Lai, 2016), and its interactions with water quality (Hamrick, 1992; Ji et al., 2007; Sinha et al., 2013), vegetation flow (Wilson et al., 2006; Marjoribanks et al., 2017), fish habitat (Kolden et al., 2016), and hydrological exchange fluxes (Zhou et al., 2018; Bao et al., 2018, 2022). All 3-D models mentioned above adopted the Reynolds-averaged Navier–Stokes (RANS) concept. More advanced models such as large-eddy simulation (LES) have also been applied for natural streams by using high-performance computers and airborne light detection and ranging (lidar)-measured high-resolution topography (Khosronejad et al., 2016; Le et al., 2019; Khosronejad et al., 2020). The differences between RANS and LES in predicting stream velocities, turbulence, and secondary flows were also carefully examined using a field-scale experimental facility as a test bed (Kang et al., 2011; Kang and Sotiropoulos, 2011, 2012).

Though significant progress has been made in modeling streamflow, new challenges emerge as we apply existing CFD techniques to mitigate the impacts of climate change and human activities on streamflow and river functions. Firstly, the modeling framework necessitates to efficiently model streamflow over large spatiotemporal scales because changes in hydrodynamics due to discharge variations often take months to decades to alter river bank structure, microbial community growth, fish life cycles, and eventually reshape river functions at grain to watershed scale (Wohl et al., 2005; Palmer et al., 2014; Wohl et al., 2015). Secondly, as applying the model at larger spatiotemporal scales usually means larger uncertainty from roughness calibration and inflow/outflow boundary condition specifications, it is necessary to develop an effective model data integration strategy such that the computational model can be better constrained by river bathymetry survey and water-stage observation data. Additionally, applying the model to large spatiotemporal scales also requires a strategy to balance computational efficiency and model accuracy.

To address the above challenges, this work demonstrates a semi-automated workflow that enables accurate and efficient 3-D CFD modeling of the streamflow in a 30 km long reach of the Columbia River spanning 9 years (Sect. 2). Specifically, a distributed hydraulic roughness calibration strategy is proposed to reduce the roughness calibration uncertainty by integrating water-stage observations, a rough wall theory, and a local roughness optimization and adjustment procedure. An integrated 1-D–3-D model approach is also adopted to reduce the uncertainty from inflow/outflow boundary condition specifications and to provide boundary conditions for

the temporal decomposition which targets computational efficiency improvement. The efficacy of the proposed workflow in calibrating roughness and predicting water stage and flow velocity during 2011–2019 is extensively demonstrated by comparing results from the present model and those from field observations in Sect. 3. Using the validated model, the relative importance of dynamic pressure to hydrostatic pressure and its dependency on discharge variations and topography heterogeneity are further investigated. The discussion on distributed roughness estimation, the model's medium- and long-term prediction performance, the relative importance of dynamic pressure, and the model's computational efficiency are given in Sect. 4.

2 Methods

2.1 River bathymetry, stage, and velocity surveys

The 30 km long reach is near the Hanford site (https://www.hanford.gov, last access: 30 January 2022) as shown (black box) in Fig. 1a. The riverbed bathymetry was measured using a lidar technique with less than 1 m resolution in vertical and 20 m resolution in horizontal directions. The measured bathymetry is then used as a geometric boundary in the CFD model. Water stage was measured in three periods at seven locations (red and yellow dots in Fig. 1b) every 10 min. For convenience, observation 1 represents the measurements at 100B, 100N, 100D, Locke Island (LI), 100H, and 100F during 2011. Observation 2 denotes the measurement at 100B during 2013 and 2014. Those measured at 100HD during 2018 and 2019 are named observation 3. These observations are then used for model calibration and validation. Specifically, water stages measured from 20 January to 16 February 2011 are used for model calibration. Measurements during the other dates in 2011 are used for short-term (less than 1 year after the calibration period) validation. Measurements during 2013 and 2014 are used for medium-term (2 to 3 years after the calibration period) validation. Those measured during 2018 and 2019 are used for long-term (7 to 8 years after the calibration period) validation. The survey at location 100HD is used to test the long-term model performance in predicting water surface elevation (WSE) outside the calibration locations. Velocity distributions were also measured at 12 cross sections (Fig. 1c) along the river on 4 March (red lines) and 1 April 2011 (blue lines) using boat-towed acoustic Doppler current profiler (ADCP) for short-term velocity validation (Niehus et al., 2014). Horizontal coordinates and bed elevation of these locations are listed in Table A1. For convenience, the horizontal coordinate at the lower-left corner of the computational domain (Fig. 1b, blue box) is converted from (564, 303.5598, 143, 735.6771 m) in the geographic information system map to (0,0) in the model domain. All vertical coordinates are referenced to the North American Vertical Datum of 1988.

2.2 Free-surface tracking and turbulence model

Quantifying water surface elevation, velocity, and bed pressure requires an accurate solution to the water–air interface and turbulent flow. In this work, OpenFOAM 5.x (CFDDirect, 2017) is used to track the water–air interface using the volume of fluid method (Hirt and Nichols, 1981; Deshpande et al., 2012) and simulate the turbulent flow using the time-averaged Navier–Stokes equations. The volume of fluid method marks a cell filled with liquid as $\alpha = 1$, filled with air with $\alpha = 0$, and partially filled liquid as $0 < \alpha < 1$. Denoting densities and viscosities of the liquid and gas by ρ_l, ρ_g, μ_l, and μ_g, then the density and viscosity of each cell is $\rho = \alpha\rho_l + (1-\alpha)\rho_g$ and $\mu = \alpha\mu_l + (1-\alpha)\mu_g$. Following these definitions, the time-averaged Navier–Stokes equations can be written as Eqs. (1) and (2). The governing equation for volume fraction α can be written as Eq. (3).

$$\nabla \cdot \boldsymbol{u} = 0 \tag{1}$$

$$\frac{\partial \rho \boldsymbol{u}}{\partial t} + \nabla \cdot (\rho \boldsymbol{u}\boldsymbol{u}) = \sigma \kappa_\alpha \nabla \alpha - \boldsymbol{g} \cdot \boldsymbol{x} \nabla \rho - \nabla p_d$$
$$+ \nabla \cdot \left[(\mu + \mu_t)\nabla \boldsymbol{u} \right] - \nabla$$
$$\cdot \left[(\mu + \mu_t)(\nabla \boldsymbol{u}^T - \frac{2}{3}\nabla \cdot \boldsymbol{u}\mathbf{I}) \right] \tag{2}$$

$$\frac{\partial \alpha}{\partial t} + \nabla \cdot (\boldsymbol{u}\alpha) + \nabla \cdot \left[\alpha(1-\alpha)\boldsymbol{u}_r \right] = 0, \tag{3}$$

where t is time, $\nabla = \frac{\partial}{\partial x}\boldsymbol{e}_x + \frac{\partial}{\partial y}\boldsymbol{e}_y + \frac{\partial}{\partial z}\boldsymbol{e}_z$ represents a spatial operator with $\boldsymbol{e}_x$, $\boldsymbol{e}_y$, and $\boldsymbol{e}_z$ denoting unit vectors along x, y, and z directions. Also denoted are time-average flow velocity ($\boldsymbol{u}$), surface tension coefficient (σ), interface curvature (κ_α), gravity acceleration ($\boldsymbol{g}$), spatial coordinate ($\boldsymbol{x}$), dynamic pressure (p_d), and dynamic turbulent viscosity (μ_t). Specifically, the interface curvature is calculated by $\kappa_\alpha = -\nabla \cdot (\frac{\nabla \alpha}{|\nabla \alpha|})$, the dynamic pressure p_d is defined as $p_d = p - \rho\boldsymbol{g}\cdot\boldsymbol{x}$ with p denoting the total pressure, $\boldsymbol{u}_r$ is the relative velocity of the liquid phase to the gas phase whose implementation in OpenFOAM can be found in Deshpande et al. (2012). The dynamic turbulent viscosity is determined by the $k-\omega$ shear stress transport (SST) model (Menter et al., 2003; Wilcox, 2006; CFDDirect, 2017).

2.3 Mesh generation and quality control

A good mesh quality is a crucial factor controlling computational stability and efficiency, especially for free-surface tracking in large-scale river modeling over a long period (Deshpande et al., 2012). In this work, the mesh is generated using a two-step generation strategy, which first generates a structured background mesh and then removes all cells totally outside a given geometry (a river bathymetry in our case). Specifically, the background mesh is generated with a horizontal mesh resolution of 20 m along x and y. Such a resolution is identical to the horizontal resolution of the lidar-measured digital elevation model (DEM). The vertical mesh
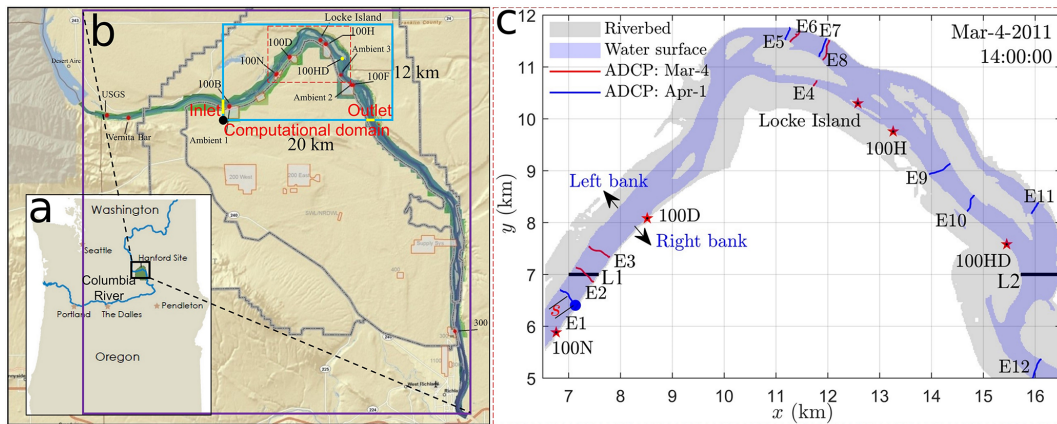
Figure 1. The location of the study site within Washington State and the Columbia River (**a**), the computational domain with the river bathymetry and water-stage survey locations (**b**), and the exact locations of velocity and stage measurements (**c**). Yellow lines in panel (**b**) represent the inlet and outlet locations of the computational domain. Red and yellow dots in panel (**b**) denote water-stage survey locations. Red and blues lines in (**c**) denote boat paths measured on two dates. Red stars and horizontal black lines in panel (**c**) represent the zoom-in of the stage survey locations in (**b**) and the locations (L1 and L2) selected to evaluate the sensitivity of stage and velocity variations to roughness heights, respectively. Panel (**a**) is a reused image of the Oregon Department of Energy (https://www.oregon.gov/energy, last access: 30 January 2022); panel (**b**) is modified from Fig. 1 in Niehus et al. (2014) produced by Sara Kallio at Pacific Northwest National Laboratory (PNNL).

resolution is set as $\Delta z = 1\,\text{m}$ by balancing modeling accuracy and computational costs. One extra mesh resolution, $20\,\text{m} \times 20\,\text{m} \times 0.5\,\text{m}$, is also created to investigate the sensitivity of modeled riverbed pressure to mesh resolution (see uncertainty analyses in Appendix A1 and Fig. A1). Figure 2 shows the horizontal and vertical mesh in the computational domain. It is observed that the aspect ratio for horizontal (x and y) grid sizes is 1, but in the vertical direction, it is 20. Figure 2c also shows that the zig-zag grid does not overlap with the riverbed, whose effect on flow is further discussed in the roughness calibration (see Sect. 2.4).

Though different from the traditional body-fitted mesh, such a zig-zag mesh strategy is both physically reasonable and technically necessary. Physically, the lidar-measured bathymetry cannot capture most geometric features that are smaller than 1 m, which means computational cells with a size less than 1 m are not necessary. In addition, the effect of geometric features on flow dynamics, either from missing features less than 1 m or the differences attributed to mesh generation, has to be calibrated using the observed water stage through a distributed rough wall model (see Sect. 2.4). The efficacy of such a meshing and calibration approach in predicting water stage and velocity is demonstrated by comparing modeled water stage and velocity with field observations (see Sect. 3.2–3.5). Technically, using grids with a high aspect ratio is usually necessary for river modeling. This is because the ratio of horizontal scales to the depth of rivers (around 1000–20 000 in this work) is usually large and a zig-zag mesh can maintain good mesh orthogonality at a large aspect ratio. By contrast, a body-fitted mesh with a large aspect ratio usually has bad mesh orthogonality, which causes

code instability for free-surface tracking and longer computational time.

2.4 Riverbed turbulence eddy viscosity and roughness parameterization

Rough elements are ubiquitous in natural rivers and have long been recognized as the major source of uncertainty in predicting river discharge, flow speed, water surface profile, and sediment transport (USACE, 1994; Smith, 2014; Powell, 2014). In this work, the effect of rough elements on turbulent flow is quantified by linking riverbed turbulence eddy viscosity to bed roughness and flow conditions through a rough wall model (Versteeg and Malalasekera, 2007).

$$\nu_t = \nu \left[\frac{\kappa y_w^+}{\ln(E y_w^+)} - 1 \right]. \tag{4}$$

Symbols in Eq. (4) denote turbulent kinematic viscosity $\nu_t = \mu_t / \rho$, kinematic viscosity $\nu = \mu / \rho$, von Karman's constant $\kappa = 0.41$, a non-dimensional wall distance $y_w^+ = \frac{y_w u_\tau}{\nu}$, and an integration constant E. Here, y_w and u_τ denote a wall distance and riverbed shear velocity. The specific value of E depends on the flow regime and the roughness parameter at the wall.

For natural rivers, the flow is usually in the fully rough turbulent flow regime. The integration value thus can be estimated by $E = E_0 / (1 + C_s k_s^+)$ with E_0, C_s, and k_s^+ denoting a constant (with a value 9.8), a roughness distribution parameter, and a non-dimensional roughness height (Schlichting, 1979; Versteeg and Malalasekera, 2007; Blocken et al., 2007; CFDDirect, 2017). As classic theories on roughness
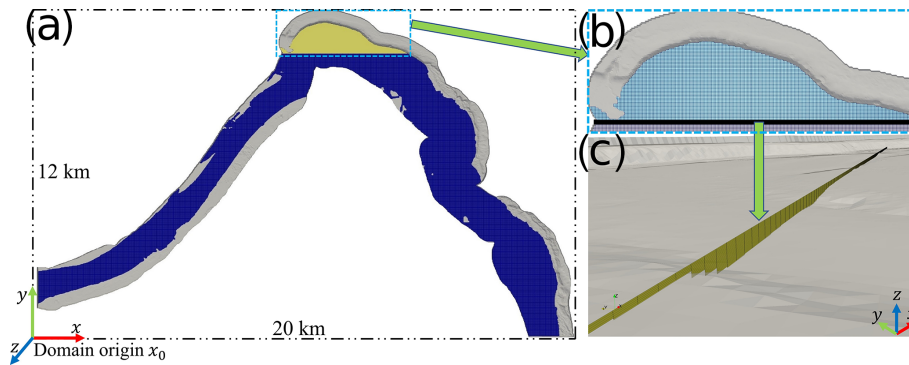
Figure 2. Horizontal and vertical computational meshes. **(a)** Top view showing the horizontal mesh over the whole domain. **(b)** Top view showing the details of horizontal mesh near LI. **(c)** 3-D view showing details of the vertical mesh structure.

are usually based on experiments of grain size roughness (Nikuradse, 1933), we choose $C_s = 0.5$ with the assumption that natural roughness distribution is similar to uniformly roughed channels as in Nikuradse's experiments (Blocken et al., 2007). Therefore, the integration value mainly depends on k_s^+, which is defined as $k_s^+ = k_s u_\tau / \nu$. Here, k_s is the roughness height that needs to be calibrated with water-stage observations.

As the bed shear velocity u_τ appears in both the non-dimensional wall distance y_w^+ and the non-dimensional roughness height k_s^+, estimation of the bed eddy viscosity shown in Eq. (4) is equivalent to estimating bed shear velocity and roughness height. In this work, the bed shear velocity is estimated using the turbulent boundary layer theory that links a non-dimensional velocity ($u^+ = u/u_\tau$) to the non-dimensional wall distance (y_w^+) through a wall function G, i.e., $u^+ = G(y_w^+)$. In the fully rough regime, the wall function follows a logarithmic law which has the form as $u^+ = \frac{1}{\kappa} \ln y_w^+ + B - \Delta B$ with $B = 5.2$ and $\Delta B = B - 8.5 + \frac{1}{\kappa} \ln k_s^+$ (Schlichting, 1979). Substituting the velocity (u^0) and wall distance (y_w^0) at the cell center closest to the wall, the wall function is converted to a non-linear function depending on shear velocity, roughness parameter, near-bed velocity, and wall distance, as shown in Eq. (5). By solving such an equation under a given roughness k_s, we can obtain the value for bed shear velocity u_τ and wall turbulent eddy viscosity ν_t.

$$G(u^0, y_w^0, u_\tau, k_s) = 0 \qquad (5)$$

The above procedure means solving for shear velocity requires an estimation of bed roughness height k_s. For straight or short rivers, a uniform roughness height may be sufficient. However, for rivers with large curvature and complex cross-sectional shapes, e.g., islands, a distributed roughness height is necessary to capture the heterogeneous distribution of bed shear velocity. This work proposes a generic approach to estimate a distributed roughness field using an error diagram and local roughness adjustment approach. The error diagram provides a rough estimation of the roughness parameters and the local adjustment further improves calibration accuracy per

the error diagram. The error diagram is based on the fact that the water surface elevation increases with increasing roughness height, and thus an optimal roughness height should fall in a range $0 < k_s < k_s^{max}$ in order for the model to match the observed water stage (Figs. 3a and A2).

In this work, the effect of rough elements larger than 1 m in the vertical direction is directly resolved by mesh and thus an upper limit of roughness can be set as $k_s^{max} = 1$ m. With such an upper limit, we run our models at eight roughness values (0, 0.025, 0.05, 0.1, 0.2, 0.3, 0.4, 0.5 m) and then calculate the mean error (ME) and mean absolute error (MAE) between modeled water stage and observed ones at six locations (Fig. 1b, red dots) from 20 January to 16 February 2011. With the error diagram as shown in Figs. 3b and A3, we calculate an optimal roughness height k_s for each observation location by making ME = 0 and MAE to be the minimum.

The optimal k_s obtained in this way is then uniformly distributed in eight regions shown in Fig. 3c. Here, k_s in R1 and R8 are identical to those in R2 and R7, respectively (Fig. 3d). Due to the interactions of flow under different roughness parameters, the locally optimized roughness field does not guarantee low modeling errors at all locations (see case OF0 in Table 1). As higher deviations occur at 100B, 100N, and 100D, their roughness parameters are systematically adjusted to achieve better accuracy for all six locations (cases OF1–OF5 in Table 1). The final calibrated roughness values at the six calibration locations are listed in case OF in Table 1. These calibrated roughness parameters are then used to simulate the flow from May to December 2011, 2013–2015, and 2018–2019 to evaluate the modeling capability for short-term, medium-term, and long-term streamflow. A more comprehensive discussion of roughness estimation and local adjustment is included in Sect. 4.1.

2.5 Boundary conditions

Temporal variations in discharge at the inlet control the dynamic changes in streamflow and riverbed conditions. Figure 4 shows the temporal variations of discharge at the in-
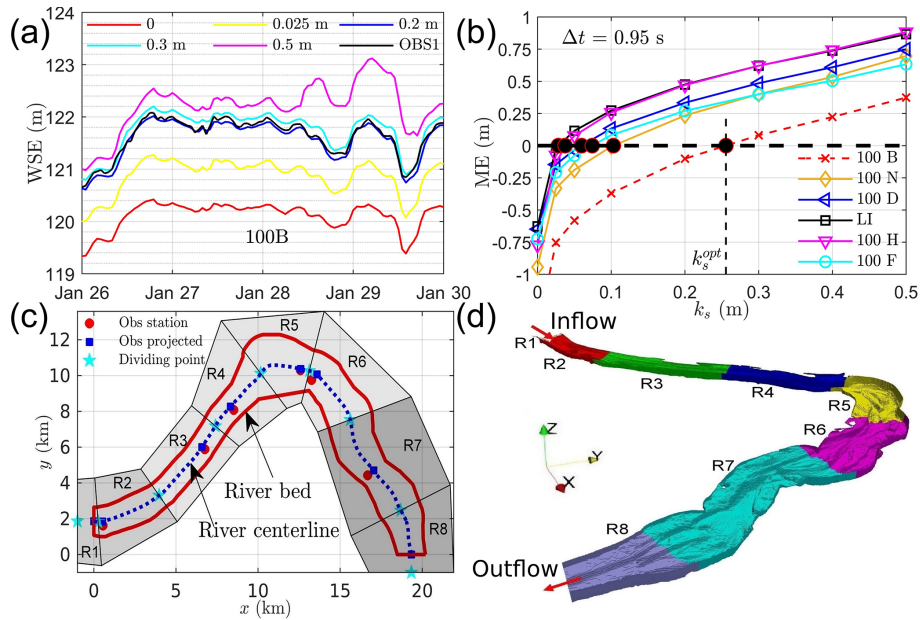
Figure 3. The effect of roughness height on WSE at a single location (a), the ME between modeled and observed WSE at six locations (b), the procedure of generating eight roughness regions (c), and the 3-D view of each region represented in mesh (d).

let during the years 2011 to 2019. A two-step approach is adopted to consider the discharge effects. Firstly, MASS1, a one-dimensional hydraulic model (Richmond and Perkins, 2009), is used to obtain the cross-sectional averaged velocity (u^1) and water stage (z^1) at 360 cross sections along a 81 km long river section (Fig. 1b, green region) during 2011–2019. Then the velocity and stage are interpolated at the inlet and outlet locations (Fig. 1b, yellow lines) as u_{in}^1, z_{in}^1 and u_{out}^1, z_{out}^1, respectively. With these data, the inlet velocity and volume fraction are calculated as $\boldsymbol{u} = (u_x, 0, 0)$ with $u_x = u_{in}^1 \frac{erf[2(z_{in}^1-z)/\Delta z]+1}{2}$ and $\alpha = \frac{erf[2(z_{in}^1-z)/\Delta z]+1}{2}$. Here, "erf" is an error function used to generate a sharp air–water interface. Other boundary conditions at the inlet are set as follows: uniform turbulence kinetic energy $k = 0.1 \, \text{m}^2 \, \text{s}^{-2}$, uniform specific dissipation rate $\omega = 0.003 \, \text{s}^{-1}$, zero gradient for dynamic pressure and turbulence eddy viscosity. It is worth mentioning that the given values of turbulent kinetic energy and specific dissipation rate have little effect on the results. At the outlet, velocity boundary condition is set as $\boldsymbol{u} = (0, -u_{out}^1, 0)$ and all other boundaries are zero gradient. At the top boundary (maximum elevation of the domain), pressure is set as 0 and the other variables are set as zero gradient. At the riverbed, the turbulence eddy viscosity is determined through a rough wall model as discussed in Sect. 2.4. A no-slip boundary condition is set for velocity and zero-gradient boundary conditions are set for dynamic pressure, volume fraction, and turbulence kinetic energy. The specific dissipation rate is calculated through $\omega_w = (\omega_{Vis}^2 + \omega_{Log}^2)^{1/2}$ with $\omega_{Vis} = \frac{6.0\nu}{\beta_1 y_w^2}$ and $\omega_{Log} = \frac{k^{1/2}}{C_\mu^{1/4} \kappa y_w}$ (see values of β_1 and C_μ in Table A2).

2.6 Spatiotemporal decomposition and initial conditions

Two spatiotemporal decomposition techniques are used in this work to improve computational efficiency. The first one is domain decomposition which decomposes the domain into 512 sub-domains and runs on 512 processors (see discussion on speedup in Sect. 4.4). Another one is time decomposition, which first divides the total simulation time, i.e., January 2013 to December 2015 and January 2018 to October 2019, into 58 months and then carries out parallel simulations for all 58 months simultaneously. The initial and boundary conditions for each month are set up at the time 4 d prior to the target simulation month. For example, to simulate the flow between 1 and 28 February, the simulation is extended to a period between 28 January and 28 February, and initial and boundary conditions are set up at the start time on 28 January. With such an approach, initial conditions for velocity, dynamic pressure, and eddy viscosity are set as zero, while for turbulence kinetic energy and specific dissipation rate are $1 \times 10^{-20} \, \text{m}^2 \, \text{s}^{-2}$ and $0.003 \, \text{s}^{-1}$ for all simulation months. The water stage and cross-sectional averaged velocity at the inlet and outlet boundaries at any time during the extended period are obtained from a one-dimensional hydraulic model as described in Sect. 2.5. It is important to note that such a spin-up approach works because (a) the flow reaches a quasi-steady state in two to three flow-through times (about $T = L/U_0 = 30\,000/0.8 \, \text{s} = 0.43 \, \text{d}$); and (b) the time-varying boundary conditions at any time are available from existing data. Further discussion on the effect of tem-
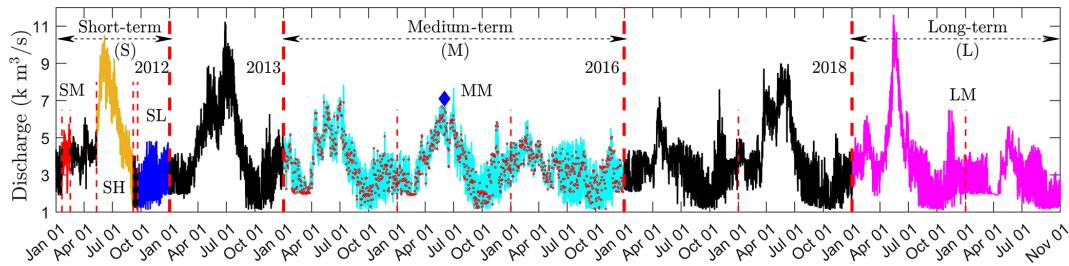
Figure 4. The time series of inlet flow rate during the years 2011–2019. S, M, and L denote short, medium, and long term. SM, SH, and SL denote the medium, high, and low flow in the short-term period; MM and LM denote mixed flow in the medium-term and long-term periods.

poral decomposition on computational efficiency is included in Sect. 4.4.

2.7 Numerical schemes and solutions

The governing equations for flow ($\boldsymbol{u}$, p_d), volume fraction (α), and turbulence (k, ω) were solved with an open-source CFD platform, OpenFOAM (version 5.x), using a finite volume method (CFDDirect, 2017). The unsteady terms are discretized with a first-order Euler scheme, the advection term of flow is discretized with a second-order Gauss linear upwind scheme, and the advection terms of turbulent kinetic energy and specific dissipation rate are discretized with a second-order Gauss linear scheme. The advection term and the compression term of volume fraction are discretized with Gauss–vanLeer and Gauss linear schemes, respectively. All diffusion terms are discretized with a corrected central differencing scheme and all gradient terms are discretized with a second-order central differencing method. With these discretization schemes, initial, and boundary conditions, Open-FOAM first updates the volume fraction at the interface using a multidimensional universal limiter with explicit solution (MULES) algorithm (Zalesak, 1979; Kuzmin et al., 2003; Liu et al., 2016) and then solves the velocity-pressure coupling using a pressure implicit with splitting of operators (PISO) algorithm (Issa, 1985), followed by solving ω and k equations. At each iteration, the discretized linear equation group for pressure is solved using a diagonal-based incomplete Cholesky preconditioned conjugate gradient (DIC-PCG) method with a relative convergence tolerance of 10^{-10}, and the discretized linear equation groups for velocity, volume fraction, turbulent kinetic energy, and specific dissipation rate are solved with a symmetric Gauss–Seidel smooth solver at a relative tolerance 10^{-10}. The initial time step is set as 10^{-10} s but allowed to adjust during runtime to not exceed 3 s. The maximum and average Courant number for all cases are less than 1.1 and 0.019, respectively. Here, the Courant number is calculated as $C_o = \Delta_t \sum_f |\phi_i| / V$ with Δ_t, $\sum_f |\phi_i|$, and V denoting the variable time step, the total fluxes of all faces, and cell volume, respectively. With the solution of volume fraction, the water surface elevation is calculated by setting $\alpha = 0.5$ (Hirt and Nichols, 1981). It is necessary to

note that the modeled water surface elevation changes little at time steps 0.1, 0.5, 0.95, 2, and 3 s (see Fig. A4); therefore, the maximum time step is chosen as 3 s to reduce computational costs.

3 Results

3.1 Short-term roughness calibration

The error diagram approach gives a rough estimation of the hydraulic roughness at each location. The modeling accuracy using these roughness parameters are -16.5–6.4 cm and 7.6–19.6 cm at six locations (case OF0 in Table 1) in terms of ME and MAE, respectively. By systematically adjusting the roughness parameters at 100B, 100N, and 100D, the overall modeling accuracy is improved. Figure 5a compares the water surface elevation using the locally adjusted roughness field (case OF in Table 1) and those from observation 1. The comparison of the hourly recorded water-stage data shows the modeled WSE accurately predicts the magnitude and frequency in the WSE. The $1:1$ plot (Fig. 5b) shows there is no systematic bias in the model, which can be further demonstrated by an R^2 and linear regression slope very close to 1 (Table 2 SM cases). Here, $R^2 = 1 - \frac{\sum (\text{WSE}_m - \text{WSE}_o)^2}{\sum (\text{WSE}_m - \overline{\text{WSE}_o})^2}$, $\overline{\text{WSE}_o} = \frac{\sum \text{WSE}_o}{N_t}$ with WSE_m, WSE_o, and N_t denoting modeled WSE, observed WSE, and the number of time series, respectively. Quantitatively, the ME at the six locations falls in the range -7.5–6.4 cm, which is equivalent to -2.7 %–2.1 % relative to the average water depth at each location (Table 2 SM cases RME). The MAE at all locations is 7.5–12.7 cm, which is equivalent to 2.1 %–5.3 % relative to water depth (Table 2 SM cases RMAE). The root mean square, defined as $\text{rms} = \sqrt{\frac{\sum (\text{WSE}_m - \text{WSE}_o)^2}{N_t}}$, for all locations is 9.2–16.4 cm, which is equivalent to 2.8 %–6.3 % relative to the average water depth at each location (Table 2 SM cases RRMS). The comparisons of the simulated water depth with observed ones are shown in Fig. 5c, d, which demonstrate similar visual and quantitative accuracies to those observed in Fig. 5a, b.
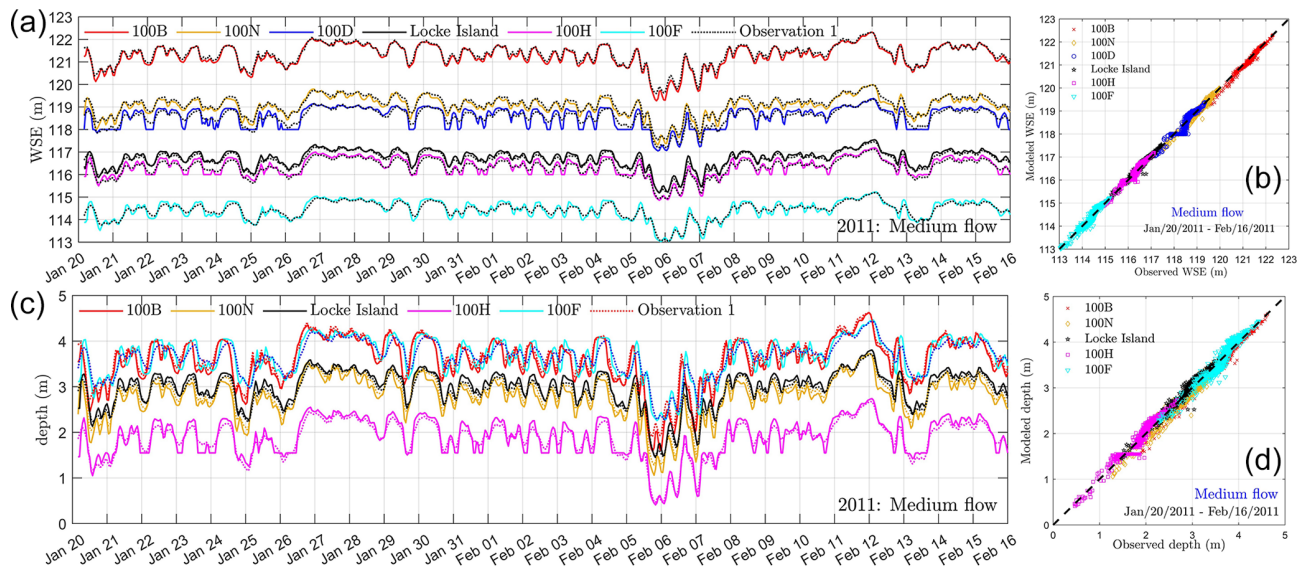
Figure 5. The comparisons of water surface elevation and depth between the model and observations using the calibrated roughness field (case OF in Table 1) during a medium flow in 2011. Panels **(a)** and **(c)** represent the hourly recorded WSE and depth, respectively. Panels **(b)** and **(d)** denote their 1 : 1 plots.

3.2 Short-term water-stage validation

Though this work calibrates the distributed roughness field using the observed WSE at a medium-flow (discharge $4227\,\text{m}^3\,\text{s}^{-1}$) scenario, we show that the calibrated roughness works well for predicting the WSE at high flow ($6335\,\text{m}^3\,\text{s}^{-1}$) and low flow ($2613\,\text{m}^3\,\text{s}^{-1}$) scenarios. Figure 6 compares the hourly recorded WSE with observations during high flow (Fig. 6a) and low flow (Fig. 6c). Figure 6b, d shows the 1 : 1 comparison between these data. The results show a good match in terms of the magnitude and frequency of the WSE at the six locations. The 1 : 1 plot shows there is no obvious bias in modeled WSE. In statistics, the ME during high flow is -2.5–$9.1\,\text{cm}$, which is equivalent to $-0.6\,\%$–$1.9\,\%$ relative to mean water depth at each location. Similarly, these values at low flow are -15.6–$5.5\,\text{cm}$ and $-7.1\,\%$–$6.6\,\%$, respectively. In terms of the MAE, it is 7.2–$13.5\,\text{cm}$ ($1.5\,\%$–$3.1\,\%$ relative to average water depth) at high flow and 13.1–$26.6\,\text{cm}$ ($5.1\,\%$–$15.8\,\%$ relative to water depth) at low flow. The rms is 9.7–$15.9\,\text{cm}$ ($2.0\,\%$–$3.8\,\%$ relative to water depth) at high flow and 17.7–$40.3\,\text{cm}$ ($6.9\,\%$–$22.2\,\%$ relative to water depth) at low flow. The calculated R^2 between the modeled and observed WSE is larger than 0.98 for six locations at high flow and is in the range 0.88–0.93 at low flow, except for at 100D where the value is 0.603. The slope of the linear regression has a similar trend to R^2 in that it falls in the range 1.05–1.1 during high and low flow at most locations; however, it has a value of 0.859 at 100D during low flow. These results suggest that the modeled WSE agrees with observation very well at all locations during the high flow event. The model WSE is less accurate at low flow and has obvious deviation at locations where the water depth

is less than $1\,\text{m}$ (case SL at 100H) or not available due to being too close to the wet–dry boundary (100D).

3.3 Short-term velocity validation

To further examine the model's predictive capability for flow velocity, Fig. 7 shows a qualitative comparison of the velocity magnitude (U) distribution at 12 cross sections between ADCP measurements and the CFD model. For instance, at cross section E1, ADCP data are placed at the left-hand side (a) and the corresponding CFD data are placed at the right-hand side (b). The distributions of velocity magnitude at other locations are arranged similarly. By comparing each pair of figures, it is found that the pattern of the distribution, e.g., locations of maximum and minimum velocity, is very similar. This means the CFD model can qualitatively reproduce the velocity distribution at each cross section. In addition, it is observed that the distribution is "cleaner" in CFD data (e.g., Fig. 7x) but shows more noise in ADCP measurements (e.g., Fig. 7w). Such a noise feature is likely induced by small-scale turbulence, measurement uncertainty from boat movement (Khosronejad et al., 2016; Le et al., 2019), and other factors such as wind shear, riparian vegetation, and inaccuracy of topography survey (Lane et al., 1999). The ADCP measurement uncertainty can also be manifested by the white space on each figure where data are lost.

Due to these problems, a more commonly used way is to compare the depth average flow velocity from ADCP and CFD models as shown in Fig. 8. The result shows that the agreement between ADCP and the simulation is very good at locations in the upstream (E1–E3) and the relatively straight downstream main channel (E9–E10) but not good at the side
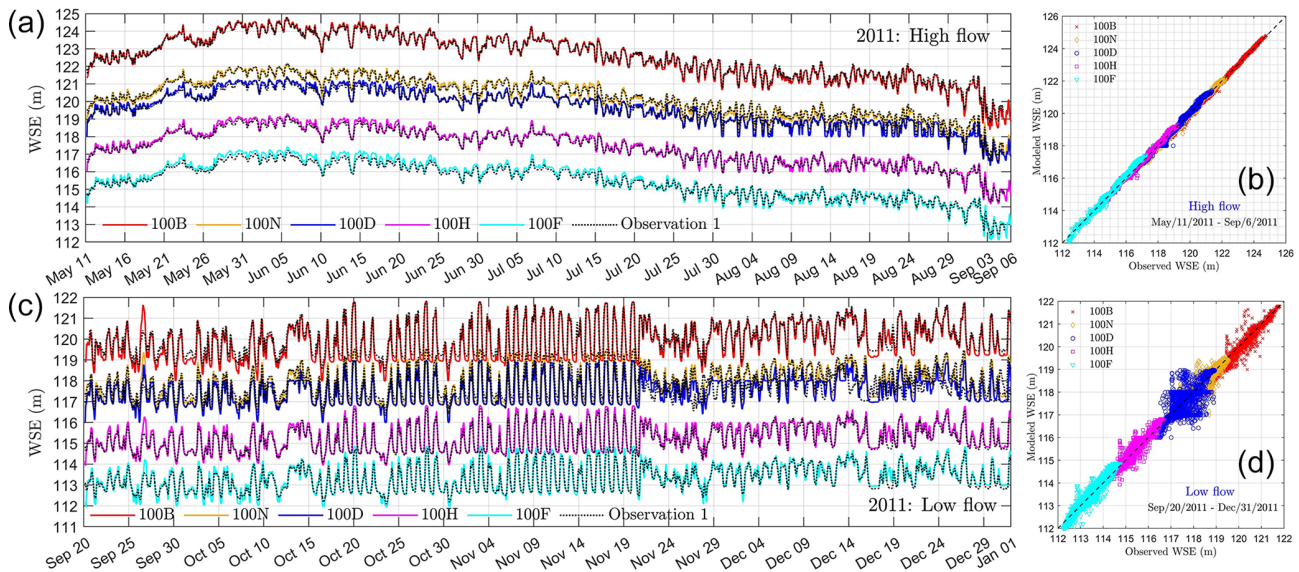
Figure 6. The comparison of water surface elevation from model and observations during high flow and low flow in 2011. **(a–b)** Hourly recorded time series of WSE and the 1 : 1 plot during high flow. **(c–d)** Hourly recorded time series of WSE and the 1 : 1 plot during low flow.

channel with large curvature (E4 and E11). The agreement is reasonably good at main channels with big curvature (E5–E8) and the outlet (E12). The corresponding correlation coefficients (R^2) between the CFD modeled and ADCP measured ones are 0.77–0.79, 0.75, 0.44–0.61, and 0.71–0.83, and 0.61 for E1–E3, E9–E10, E4/E11, E5–E8, and E12, respectively. As R^2 of around 0.8 is usually recognized as an "acceptable" or "good" result in previous work (Nicholas and Sambrook Smith, 1999; Lane et al., 1999; Horritt, 2005; Lane et al., 2005); this means that the flow velocity predicted by the CFD model at most of the locations (9 out of 12) is reliable for practical applications. It is worth mentioning that the modeling accuracy for flow velocity may not be further improved by using more advanced CFD modeling or more refined mesh without improving the accuracy of ADCP and topography survey. For instance, Le et al. (2019) conducted a large-eddy simulation for a 3.2 km long reach of the Mississippi River with a given discharge, the prediction accuracy of velocity was not improved when compared to ADCP measurements even though 109 million grid and 38 400 CPU hours were used to reach a steady state. Furthermore, as the two dates chosen for velocity validation are randomly selected, it may be reasonable to expect that flow velocity modeling at other dates likely has similar accuracy, at least for short-term scenarios. This claim may be indirectly backed by the fact that WSE calibrated during 2011 still has a similar accuracy to that in 2018 and 2019 (see Sect. 3.5).

3.4 Medium-term water-stage validation

The short-term water-stage validation shows the roughness calibrated using the WSE observed at a medium flow can well predict WSE at medium-, high-, and low-flow scenar-

ios. To further test if the calibrated roughness can be applied for medium-term (2 to 3 years after the calibration period) surface flow simulations, Fig. 9 compares the modeled WSE with the observed WSE at 100B during 2013–2014. Figure 9a shows a comparison of the hourly recorded WSE from the model with those from two different observations. Such a comparison shows that the modeled WSE agrees well with the observations from 1 January 2013 to 1 August 2014. In addition, it shows that observed WSE has uncertainties. A further comparison between the two observations shows that WSE from observation 2 is about 3.2 cm higher than that from observation 1 and that a small shift in time results in a large error in standard deviation between the two observations (see uncertainty analyses in Appendix A2 and Fig. A7). However, as observation 1 lacks the record during 2013–2014, observation 2 is used for validation during this time period.

As WSE observation is missing at some dates, three time periods with continual observations (see MH^2 and ML^2 in Table 2) were chosen to illustrate the modeling performance in predicting WSE as shown in Fig. 9b, c, d. The comparison shows that the modeled WSE agrees very well with observations at the high flow scenarios during March–June 2013 (Fig. 9b) and April–July 2014 (Fig. 9d). The ME, MAE, and rms during these periods are −10.1 to −9.2 cm, 10.5–11.9 cm, and 13.3–15.1 cm, respectively. The corresponding relative error to average water depth is −2.8 % to −2.2 %, 2.5 %–3.3 %, 3.1 %–4.1 %, respectively. At the low flow during September 2013–January 2014 (Fig. 9c), the model shows a larger error especially when the WSE is low (close to 119 m). However, the relative errors to water depth, with values of −9.9 %, 10.7 %, and 12.6 % for ME,
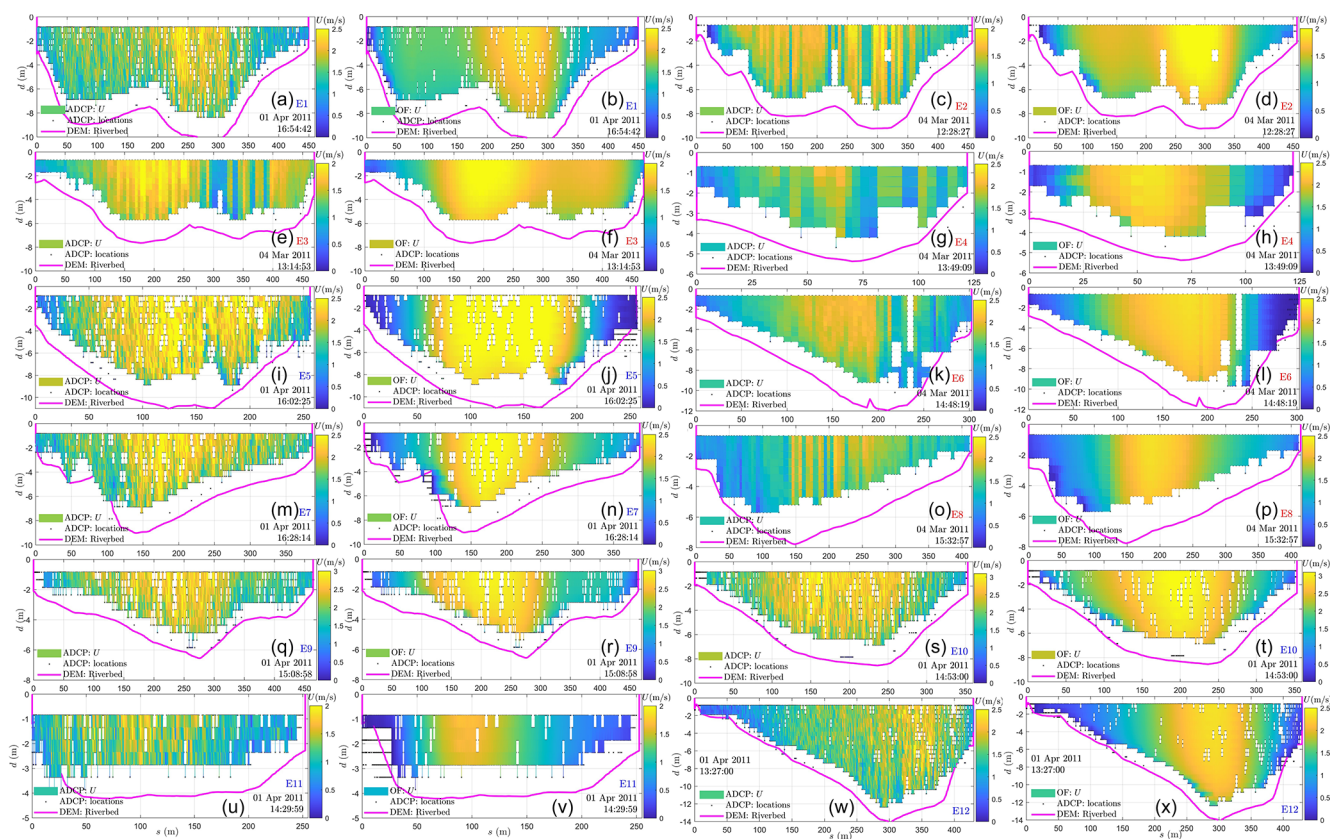
Figure 7. The velocity magnitude distributions on cross sections E1–E12 from ADCP surveys (columns 1 and 3) and CFD modeling (columns 2 and 4). Cross-section names (E1–E12) with red and blue color denote survey dates on 4 March and 1 April 2011, respectively. Symbols d and s denote depth away from the water surface and distance from the right bank (see Fig. 1c), respectively.

MAE, and rms (see ML^2 in Table 2), are still low. Figure 9e, f, g further shows a 1 : 1 comparison between modeled and observed WSE. The R^2 and the linear regression slope are 0.88–0.98 and 1.06–1.1, respectively. These results suggest the predicted WSE has no obvious bias and the prediction has good accuracy for a medium-term prediction.

3.5 Long-term water-stage validation

The long-term (7 to 8 years after the calibration period) performance of WSE prediction is important for predicting river corridor function under a long-term climate change scenario. To test the modeling performance for long-term WSE prediction, Fig. 10 compares the WSE from the model and the observation at one location (yellow dot in Fig. 1b), different from the locations used for calibration. Fig. 10a shows that the model well captures the trend of the fluctuation in WSE at 100HD during August 2018–November 2019. The ME and MAE are 7.2 and 14.9 cm, respectively. This is equivalent to 5.4 % and 11.3 % relative to the mean water depth. The rms is 22.5 cm and about 17.0 % relative to the average water depth at 100HD during August 2018–November 2019. Figure 10b further shows the 1 : 1 plot between the modeled and

observed WSE at 100HD. The R^2 and linear regression slope are 0.89 and 0.980, respectively. These statistics show there is no obvious bias in our model as the slope is very close to 1. As the flow during August 2018–November 2019 is always low (2580 m^3 s^{-1}), the R^2 during this time period is similar to those calculated at low flow scenario (see SL at 100B–100F in Table 2) in 2011–2015. Similarly, a lower R^2 is also related to a small time shift in the observation as shown in Fig. A7. Considering that a small time shift in the observation results in a significant error in MAE and rms, the ME is a more reliable index for evaluating the modeling accuracy. Therefore, it is reasonable to claim that our model can predict WSE in 2018 and 2019 with an accuracy of 5.4 % relative to mean water depth using the roughness calibrated in 2011. This suggests that in the next 9 years the WSE may be reliably predicted using the calibrated roughness at the present time. The water depth is another commonly used metric for the hydrodynamics model evaluation. Figure 10c, d show the comparisons of water depth from the model and observation at 100HD. It is observed that these results demonstrate identical visual and quantitative accuracy to those quantified by WSE.
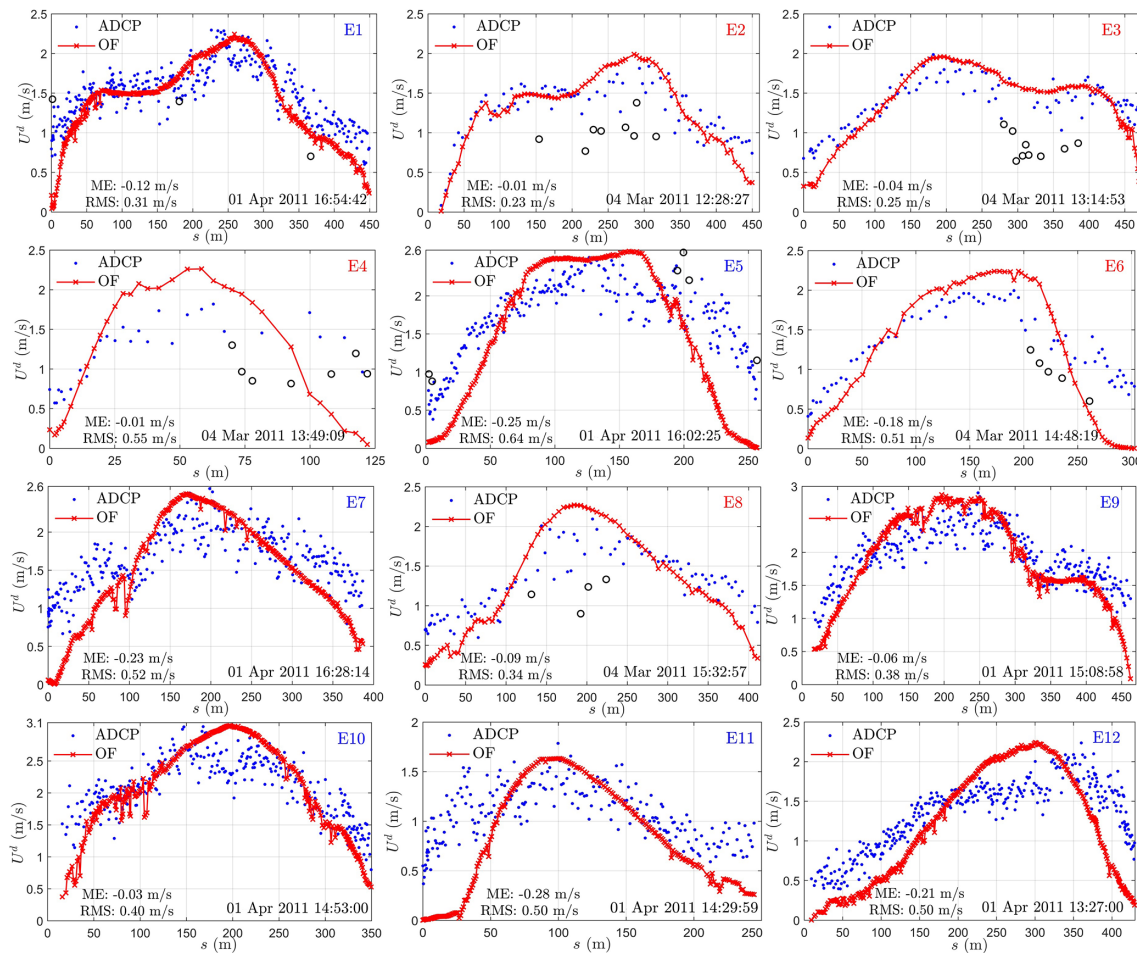
Figure 8. The comparison of depth-averaged velocity magnitude determined from ADCP surveys and CFD modeling. Black circles denote measured velocity outliers visually determined through velocity components (Figs. A5 or A6).

3.6 The ratio of dynamic pressure to static pressure

The dynamic pressure is important streamflow quantify, especially for environmental and ecological functions. However, modeling results of dynamic pressure in large-scale natural rivers are rarely reported and the relative importance of dynamic pressure to hydrostatic pressure is also not clear. To quantitatively understand the relative importance of dynamic pressure to the hydrostatic pressure, we define their ratio as $r = p_d/[\rho g(\text{WSE} - z_b)]$, with WSE and z_b denoting the water surface elevation and riverbed elevation. As such a ratio varies with location and discharge, we categorize the ratio into five ranges, including -0.4 to -0.3, -0.3 to -0.2, -0.2 to -0.1, -0.1–0, and 0–0.1. We then calculate the area (A_r) of which the pressure ratio falls in each range and its relative ratio to the total wetted area (A_T). Figure 11 shows the variations of the relative pressure ratio area (A_r/A_T) with time (a) and discharge (b), as well as the spatial distribution of each pressure ratio range at low- (c), medium- (d), and high-flow (e) conditions. The results (Fig. 11a) show that 60 %–

80 % of the riverbed is covered with dynamic pressure whose value is -10 % to 0 of the hydrostatic pressure, while 10 %–30 % of the total area is covered with dynamic pressure is of -20 % to -10 % of the hydrostatic pressure. The region with a dynamic pressure ratio higher than 0 or less than -20 % is small. In addition, it was observed from Fig. 11b that the relative pressure ratio area (A_r/A_T) behaves differently when the discharge is less than 2000 m^3 s^{-1} (low flow), between 2000 and 4000 m^3 s^{-1} (medium flow), and larger than 4000 m^3 s^{-1} (high flow), respectively. Specifically, the blue color is observed at both the dry–wet boundary and main channel at a low flow (Fig. 11c), while it is mainly observed at the dry–wet boundary at a high flow (Fig. 11e). At a medium flow, the blue area can be observed in both the main channel and the dry–wet boundary, though its area is obviously smaller than that observed in the low flow scenario. According to Fig. 11a, b, the blue area could increase from around 10 % at a high flow to around 30 % at a low flow. This means that dynamic pressure may be important at both the dry–wet boundary and the main channel at low-flow conditions.
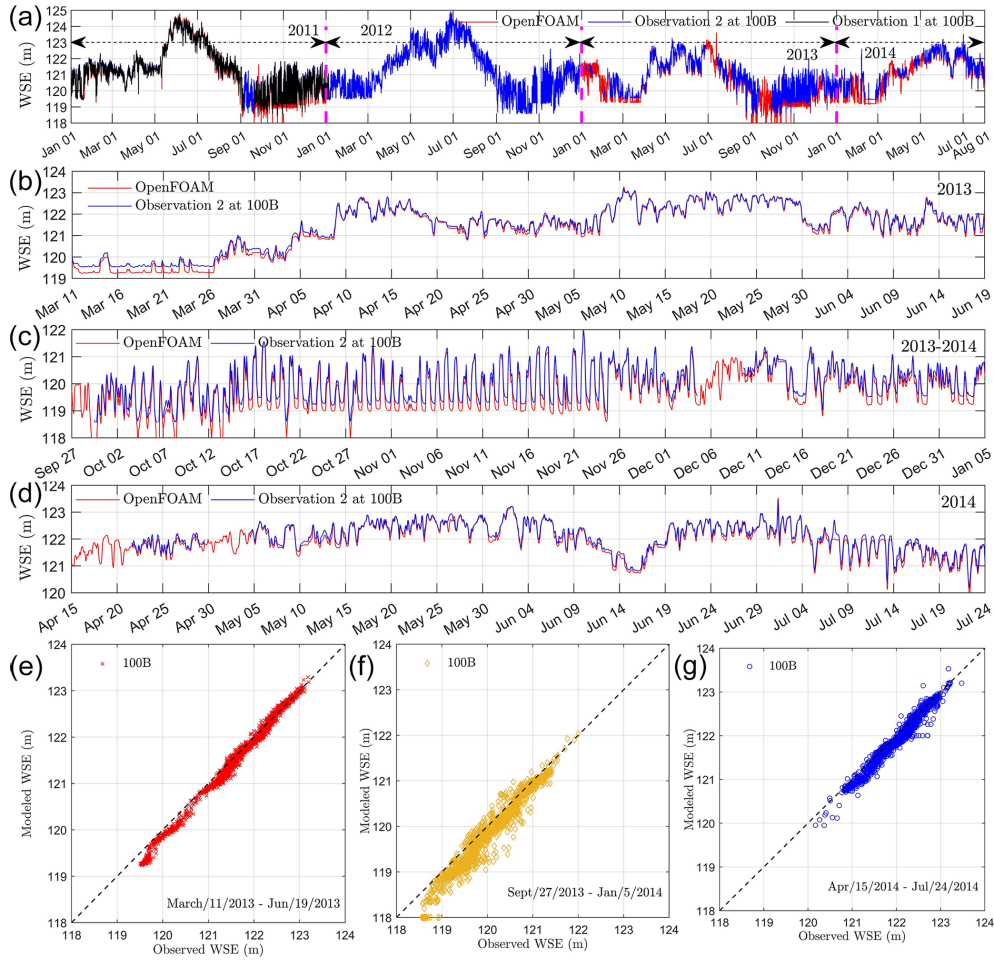
Figure 9. Medium-term model validation for water surface elevation. A comparison of hourly recorded WSE from model and observations during 2011–2014 **(a)**, medium flow **(b)**, low flow **(c)**, and high flow **(d)**. Panels **(e)**–**(g)** denote the 1 : 1 plot during medium-, low-, and high-flow scenarios.
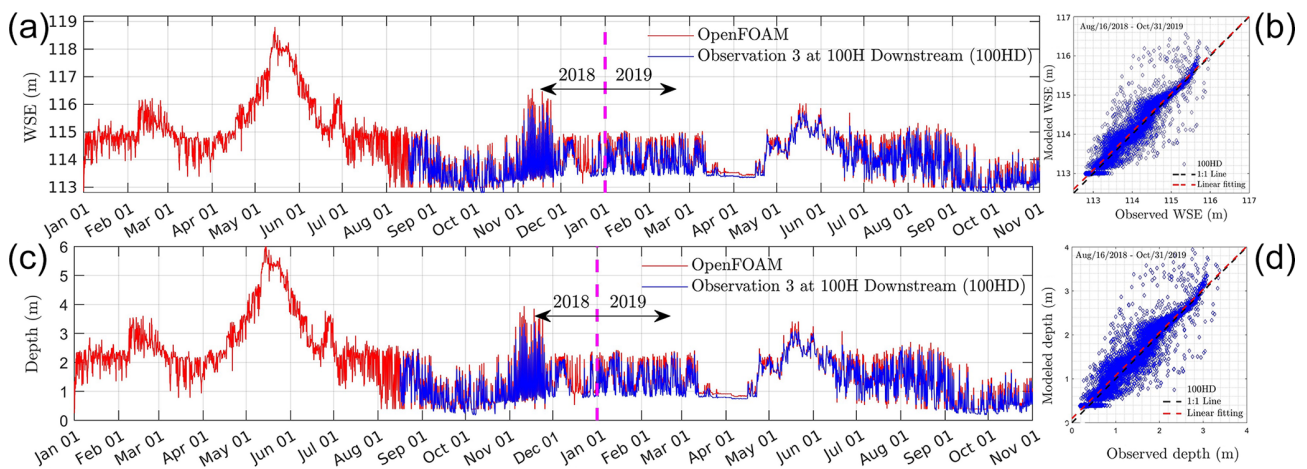

Figure 10. Long-term model validation for water surface elevation and depth. A comparison of the hourly recorded WSE and depth from model and observations at 100HD during 2018–2019 **(a, c)** and their 1 : 1 plots **(b, d)**.
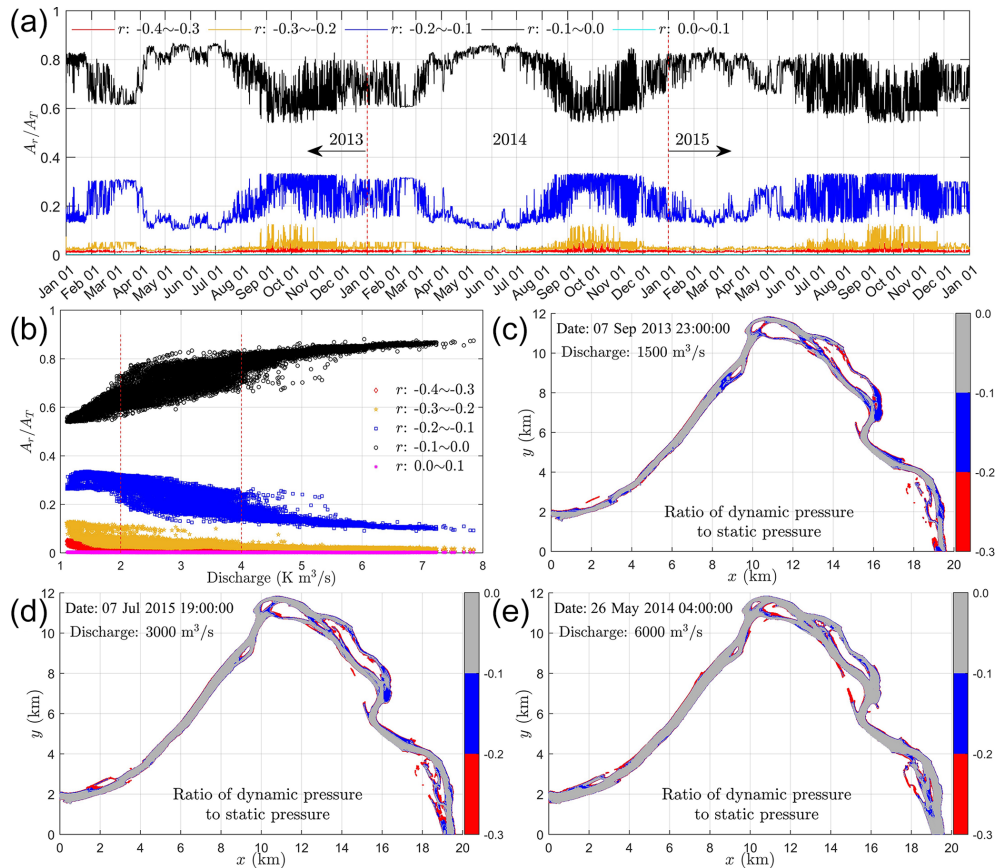
Figure 11. The variations of the relative pressure ratio area (A_r/A_T) with time **(a)** and discharge **(b)**, as well as the spatial distribution of each pressure ratio range at low- **(c)**, medium- **(d)**, and high-flow **(e)** conditions.

4 Discussion

4.1 Distributed hydraulic roughness estimation for large-scale rivers

Hydraulic roughness is a metric used to estimate the resistance applied to flow from complex sediment structures. Such a value controls the flow speed and water surface elevation and has been long recognized as the primary control of the accuracy of numerical modeling of natural rivers (US-ACE, 1994). For small-scale rivers, assuming a uniformly distributed roughness is usually acceptable. For large-scale rivers, however, it is necessary to use a distributed roughness height because the interactions between flow and local topographic features vary with locations. To guide roughness estimation in practical applications, we give an in-depth discussion on the roughness estimation approach used in the present work (Sect. 4.1.1–4.1.2) and its connections to other approaches such as Manning's coefficient (Sect. 4.1.4) and streambed microtopography (Sect. 4.1.5).

4.1.1 Calibration with observations: local optimal roughness height

Roughness calibration with observed water stage is an efficient approach for roughness estimation in 3-D free-surface models. The physical basis of this approach is that the bulk flow velocity in streams is monotonically related to bed roughness and therefore an optimal roughness can be obtained by monotonically adjusting a roughness parameter to match modeled WSE with observed ones. Usually, a very small roughness height, e.g., 0, results in an underestimation of WSE. While a high roughness height, e.g., the size of the biggest sediment, results in an overestimation of WSE. With this in mind, a series of numerical experiments can be designed by systemically adjusting the roughness parameter from 0 to the biggest value. And the relative error between modeled WSE and observed ones can be directly calculated as shown in Fig. 3b. An optimal roughness parameter for each observation location can then be obtained, which is here referred to as a locally optimal roughness height.

Using such an approach, it is generally observed that the modeled WSE is very sensitive to the given roughness height when its value is much smaller than the optimal one (see

Table 1. Roughness adjustment approach and associated ME and MAE.

Case name	Calibrated k_s (cm)						ME during 20 Jan–16 Feb 2011 (cm)							MAE during 20 Jan–16 Feb 2011 (cm)						
	100B	100N	100D	LI	100H	100F	100B	100N	100D	LI	100H	100F	Range	100B	100N	100D	LI	100H	100F	Range
OF0	25.56	10.3	5.98	2.83	3.74	7.42	−16.5	−19.5	−6.8	6.4	4.8	0.3	16.5–6.4	16.5	19.6	12.7	7.6	8.9	9.3	7.6–19.6
OF1	30	10.3	5.98	2.83	3.74	7.42	−11.1	−19.5	−7.4	6.4	3.3	0.3	19.5–6.4	11.2	19.6	13.4	7.6	10.1	9.3	7.6–19.6
OF2	40	10.3	5.98	2.83	3.74	7.42	−0.6	−19.5	−7.4	6.4	3.3	0.3	19.5–6.4	5.8	19.6	13.4	7.6	10.1	9.3	7.6–19.6
OF3	40	10.3	5.98	2.83	3.74	7.42	1.6	−16.8	−7.2	6.4	3.4	0.4	16.8–6.4	6.5	17.0	13.3	7.6	10.1	9.3	7.6–17.0
OF4	30	18.6	5.98	2.83	3.74	7.42	−8.7	−16.9	−7.4	6.4	3.3	0.3	16.9–6.4	9.1	17.0	13.3	7.5	10.1	9.2	7.5–17.0
OF5	30	18.6	9.0	2.83	3.74	7.42	−7.5	−11.7	−3.6	6.4	3.3	0.3	11.7–6.4	8.2	12.2	12.6	7.5	9.2	9.2	7.5–12.6
OF	30	18.6	12.0	2.83	3.74	7.42	−6.6	−7.5	−0.6	6.4	3.3	0.3	7.5–6.4	7.7	8.9	12.7	7.5	10.0	9.2	7.5–12.7
OFK1	12.2	12.2	12.2	12.2	12.2	12.2	−29.1	6.6	17.7	32.1	31	13.1	29.1–32.1	29.1	7.5	19.5	32.6	31.5	14.6	14.6–29.1
OFK2	25.56	6.25	6.25	6.25	6.25	6.25	−16.7	−15.0	1.3	14.8	12.2	13.1	16.7–14.8	16.7	15.2	12.2	15.1	13.4	9.2	9.2–15.2
OFK50	see Fig. A8						−19.4	−18.8	−6.1	8.5	8	1.4	19.4–8.5	19.4	18.8	12.5	9.3	10.5	9.7	9.3–19.4
MS	30.5	18.6	15.6	3.9	3.9	7.42	−4.7	−1.2	4.9	7.7	3.9	0.3	4.7–7.7	6.7	6.4	13.9	8.6	10.3	9.2	6.4–13.9
MS2	30.5	18.6	12.0	3.9	3.9	7.42	−5.6	1.9		7.7	3.8	0.2	5.6–7.7	7.1	7.8	12.9	8.5	10.2	9.2	7.1–12.9
MS3	30.5	18.6	9.0	3.9	3.9	7.42	−6.6	−9.8	−1.0	7.7	3.8	0.2	9.8–7.7	7.6	10.6	12.5	8.6	10.2	9.2	7.6–12.5

Fig. 3a, b, and Figs. A2 and A3). For example, the ME increases by about 0.5–0.7 m when the roughness height increases from 0 to 0.025 m (Fig. 3b). However, further increasing the roughness height from 0.025 to 0.05 m results in much smaller changes (0.1–0.18 m) in WSE compared to that of changing from 0 to 0.025 m. These changes are even smaller when the roughness height approaches the optimal value. These behaviors can be explained as follows.

Firstly, setting a zero roughness height is equivalent to using a smooth wall function (Versteeg and Malalasekera, 2007; CFDDirect, 2017). Such treatment is only valid when the shape, size, and distribution of individual sediments on the riverbed are explicitly represented by the riverbed topography. For almost all CFD modeling of natural rivers, however, the details of individual sediments cannot be measured as the commonly used survey technology, i.e., lidar, cannot capture geometric details smaller than a half meter (Podhorányi et al., 2013; Tonina et al., 2019). Therefore, setting a zero roughness height on top of a lidar-measured topography results in large errors in predicting WSE when compared to observed ones. By contrast, using a non-zero roughness value considers the effects of the missing geometric details on flow, which makes the model more approaching to the real situation. This can be demonstrated by similar values of the optimal roughness heights, i.e., 2.83–25.56 cm (Table 1, case OF0), to typical sizes of gravel and cobbles (2 mm–0.256 m) (Berenbrock and Tranmer, 2008). Hence, it can be concluded that the roughness wall model and non-zero roughness heights reduce the sensitivity of WSE to roughness height; and they provide a reliable mechanism for roughness calibration. It is worth mentioning that the sensitivity of WSE to roughness height can be further reduced if details (mm-scale) of individual sediments on riverbed can be measured and explicitly represented by sufficiently small (mm-scale) mesh in the CFD model (Lane et al., 2004; Hardy et al., 2005). However, measuring a river topography and generating a mesh with mm resolution is currently impractical for large-scale natural streams. Our approach discussed here, therefore, is still of great practical importance.

4.1.2 Calibration with observations: local roughness adjustment

As the roughness parameter calibrated in Sect. 4.1.1 usually works well for a single location, this means that applying such a parameter to other locations cannot guarantee overall modeling accuracy for all locations. Different strategies can be applied to solve this problem. The simplest strategy is to choose one roughness parameter and apply it uniformly to the whole domain. Such a parameter can be directly identified from error diagrams (Fig. 3b or Fig. A3), which has a value of $k_s^1 = 12.2$ cm. Using this strategy, the overall modeling accuracy is about −30–30 cm and 7.5–30 cm in terms of ME and MAE (see OFK1 in Table 1). The second strategy is to decompose the riverbed into two regions

Table 2. A summary of flow scenario, discharge, water depth, roughness height, and modeling accuracy for calibration, validation, and prediction.

Survey station	Time period	Year	Month/ day	Flow scenario	Mean discharge (m^3 s^{-1})	Mean depth (m)	k_s (cm)	ME (cm)	RME (%)	MAE (cm)	RMAE (%)	rms (cm)	RRMS (%)	R^2	β
											WSE difference between OF and observed				
100B	SM	2011	1/20–2/16	Medium	4227	3.57		−6.6	−1.8	7.7	2.1	10.1	2.8	0.963	1.072
	SH	2011	5/11–9/6	High	6335	4.88		−2.1	−0.4	7.2	1.5	9.7	2.0	0.994	1.062
	SL	2011	9/20–12/31	Low	2613	2.19		−15.6	−7.1	19.7	9.0	25.4	11.6	0.914	1.102
	MH^2	2013	3/11–6/19	High	4449	3.65	30	−10.1	−2.8	11.9	3.3	15.1	4.1	0.982	1.083
	ML^2	2013–14	9/27–1/5	Low	2517	2.10		−20.7	−9.9	22.4	10.7	26.4	12.6	0.879	1.108
	MH^2	2014	4/15–7/24	High	5217	4.27		−9.2	−2.2	10.5	2.5	13.3	3.1	0.945	1.053
	MM^2	2013–14	1/1–8/1	Mixed	3755	3.12		−14.4	−4.6	16.1	5.2	22.1	7.1	0.965	1.065
100N	SM	2011	1/20–2/16	Medium	4227	2.78		−7.5	−2.7	8.9	3.2	10.9	3.9	0.943	1.031
	SH	2011	5/11–9/6	High	6335	3.96	18.6	−2.5	−0.6	8.9	2.2	11.0	2.8	0.991	1.058
	SL	2011	9/20–12/31	Low	2613	1.58		−10.3	−6.5	19.9	12.6	26.1	16.4	0.881	1.061
	MM	2013–15	1/1–12/31	Mixed	3424	2.17		NA	NA	NA	NA	NA	NA	NA	NA
100D	SM	2011	1/20–2/16	Medium	4227	NA		−0.6	NA	12.7	NA	16.4	NA	0.874	1.149
	SH	2011	5/11–9/6	High	6335	NA	12	3.1	NA	10.6	NA	13.7	NA	0.983	1.071
	SL	2011	9/20–12/31	Low	2613	NA		−1.8	NA	26.6	NA	40.3	NA	0.603	0.859
	MM	2013–15	1/1–12/31	Mixed	3424	NA		NA	NA	NA	NA	NA	NA	NA	NA
LI	SM	2011	1/20–2/16	Medium	4227	2.99		6.4	2.1	7.5	2.5	9.2	3.1	0.948	1.023
	SH	2011	5/11–9/6	High	6335	4.02	2.83	NA	NA	NA	NA	NA	NA	NA	NA
	SL	2011	9/20–12/31	Low	2613	1.91		NA	NA	NA	NA	NA	NA	NA	NA
	MM	2013–15	1/1–12/31	Mixed	3424	2.44		NA	NA	NA	NA	NA	NA	NA	NA
100H	SM	2011	1/20–2/16	Medium	4227	1.90		3.3	1.7	10.0	5.3	12.0	6.3	0.923	1.073
	SH	2011	5/11–9/6	High	6335	3.00	3.74	5.7	1.9	9.2	3.1	11.3	3.8	0.989	1.053
	SL	2011	9/20–12/31	Low	2613	0.83		5.5	6.6	13.1	15.8	18.4	22.2	0.922	1.062
	MM	2013–15	1/1–12/31	Mixed	3424	1.36		NA	NA	NA	NA	NA	NA	NA	NA
100F	SM	2011	1/20–2/16	Medium	4227	3.66		0.3	0.08	9.2	2.5	11.5	3.1	0.928	1.106
	SH	2011	5/11–9/6	High	6335	4.77	7.42	9.1	1.9	13.5	2.8	15.9	3.3	0.978	1.103
	SL	2011	9/20–12/31	Low	2613	2.59		2.6	1.0	13.3	5.1	17.7	6.9	0.926	1.071
	MM	2013–15	1/1–12/31	Mixed	3424	3.12		NA	NA	NA	NA	NA	NA	NA	NA
100HD	LL^3	2018–19	8/16–10/31	Low	2580	1.33	NA	7.2	5.4	14.9	11.3	22.5	17.0	0.89	0.980
	LM^3	2018–19	1/1–10/31	Mixed	3310	1.78		7.2	4.0	14.9	8.4	22.5	12.6	NA	NA

Observation stations are illustrated in Fig. 1b. The first character in "time period" represents short-term (S), medium-term (M), and long-term (L), and the second character in "time period" represents medium-(M), high- (H), low- (L), or mixed-type-flow (M) scenarios. Superscripts 2 and 3 denote observation data used for comparison are from observation 2 and observation 3. R^2 and β is a coefficient quantifying the degree of correlation between modeled and observed WSE and the slope of the linear regression of 1 : 1 plots. NA is used when observed data are not available.

with different roughness parameters assigned to each region. This strategy is based on the fact that the error diagrams (Fig. 3b or Fig. A3) show two different behaviors at the region 100B and the other five locations. Following this concept, $k_s^{2b} = 25.56$ cm is assigned for the region at 100B and $k_s^{2a} = 6.25$ cm is assigned for all other regions. The overall modeling accuracy for WSE using such a strategy is around −17–15 cm and 9–15 cm in terms of ME and MAE (see OFK2 in Table 1). Overall, we see that the modeling accuracy of using one or two roughness values is ±0.3 and ±0.15 m in terms of ME, and 0.3 and 0.15 m in terms of MAE. It is important to mention that such a modeling accuracy can be roughly predicted using error diagrams without running actual simulations (cases OFK1 and OFK2 in Table 1). This means that the error diagram is a good tool for designing a calibration strategy. We also tested the strategy of interpolating the locally optimal roughness height to 50 uniformly distributed regions (see k_s and regions in Fig. A8). The overall accuracy for WSE is −19.4–8.5 cm and 9.3–19.4 cm in terms of ME and MAE (case OFK50 in Table 1), respectively. This result suggests that interpolating the locally optimal rough-

ness height to more regions does not improve modeling accuracy because roughness interpolating itself may introduce extra uncertainty to the roughness field. From the above discussion, we found that the best strategy is to decompose the riverbed into N regions with N equal to the number of survey locations. Without further adjustment of the local optimal roughness parameters, such a strategy gives an overall modeling accuracy of WSE as −16.5–6.4 cm and 7.6–19.6 cm in terms of ME and MAE, respectively.

To further improve the modeling accuracy, local adjustment of the local optimal roughness parameters is necessary. This is because the locally optimal roughness parameters neglect the flow interactions due to locally variable flow resistance, backwater effects from downstream to upstream, and the effects of sinuosity. The local adjustment is used to incorporate these effects into the calibration and achieve a globally optimal roughness calibration. As higher uncertainty (case OF0 in Table 1) occurs at the upstream locations (100B, 100N, and 100D) using the locally optimal roughness height, we systematically adjust the roughness parameters at these locations. The final modeling accuracy for WSE is

−7.5–6.4 cm and 7.5–12.7 cm in terms of ME and MAE, respectively. Further improvement of the accuracy is possible but not necessary as the relative errors to water depth have been reduced to −2.7 %–2.1 % and 2.1 %–5.3 % in terms of ME and MAE.

Nevertheless, it is worth summarizing how local adjustment improves modeling accuracy. Firstly, increasing roughness height at the most upstream location (100B) improves the accuracy of WSE only at that location (see OF0, OF1, and OF2 in Table 1). Secondly, changing roughness height at 100N has little effect on WSE at 100N and neighboring upstream locations (see OF2 and OF3 in Table 1). And thirdly, increasing roughness height at 100D significantly affects WSE at all upstream locations and has a larger influence on the locations closer to that location. These results suggest that roughness heights at some critical locations (most upstream and close to pool) have a larger impact on the overall modeling accuracy. It is also worth noting that the calibration strategy discussed in Sect. 4.1.1–4.1.2 is designed based on water-stage measurement data availability. Such a strategy can provide unique roughness values in the local optimal roughness calibration step, however, may not provide unique values in the local roughness adjustment step. Considering that the overall model performance is controlled by both steps, future applications are recommended to pay more attention to the first step due to its uniqueness. Specific actions include deploying stage survey devices at critical locations (upstream, pools, bends, islands, etc.) and in characteristic sediment environments, e.g., gravel, sand, mixed gravel and sand, and vegetation. With a better distribution of the stage survey locations, the overall model accuracy solely based on the first step is likely significantly improved, consequently the local roughness adjustment step becomes less important. If the adjustment step is a must, integrating the present CFD framework with machine learning approaches, e.g., parameter learning (Tsai et al., 2021) and reinforcement learning, can potentially address the non-uniqueness issue.

4.1.3 Sensitivities of water surface elevation and velocity magnitude variations to roughness heights

Though the above roughness estimation strategy only targets minimizing the water-stage differences between the model and observations at six locations, it is worth noting that the roughness values also affect the spatial variations of water stage and velocity. By selecting case OF (see Table 1) as a reference case, Fig. 12 compares the distributions of water stage and free-surface velocity magnitude from the reference case with those cases using different uniform roughness heights at two transects (L1 and L2) (see Fig. 1c). In particular, Fig. 12a shows that the average WSE at transect L1 increases from 118.4 to 120 m with the roughness height increasing from 0 to 0.5 m. This contributes to only an 18 % increase in the water depth at the channel thalweg (eleva-

tion 109.4 m); however, it significantly affects the model accuracy in predicting the water depth near the river banks where the submerged bed elevation from the reference case is around 119 m. At transect L2 (Fig. 12d), increasing the roughness height from 0 to 0.5 m causes an increase in WSE from 113.9 to 115.7 m if selecting the yellow circles as the average WSEs. This means the water depth at the channel thalweg increases 28 % (bed elevation of 107.55 m) and also causes significant changes in the water depth near the banks whose elevation is around 115 m. Figure 12d also shows that the spatial variation of WSE is affected by the selection of roughness parameters, especially at a lower value. In summary, the water depth near the river banks is highly sensitive to the roughness values, while the sensitivity is reduced when approaching the river thalweg. Due to such a reason, the model calibration should pay more attention to the comparison of water stage from model and observations at river bank regions.

Because velocity at the water surface is a good indicator of the velocity distribution below the surface, Fig. 12b compares the distribution of surface velocity magnitude at transect L1 under different roughness heights. The result shows that the velocity distribution from the zero roughness case differs significantly from the other cases with non-zero roughness heights. For the cases with non-zero roughness heights, increasing the roughness value (from 0.025 to 0.5 m) does not significantly affect the spatial distribution of velocity, however, reduces its maximum value from 2.46 to 1.92 m s^{-1} (22 % decrease). The relative error (r_U) of the maximum velocity between these cases and the reference case for L1 is shown in Fig. 12c from which the relative error is observed to decrease from 10 % to around −15 % with increasing roughness heights. Similar behaviors can be observed at L2 as shown in Fig. 12f. With the roughness height increasing from 0.025 to 0.5 m, the maximum velocity is reduced from 2.68 to 1.88 m s^{-1}, while the relative error r_U decreases from around 10 % to −20 %. From these results, we conclude that the distribution of surface velocity is not sensitive to the non-zero roughness heights but its maximum value could vary 25 %–30 % for the roughness range considered here.

Interestingly, it is observed that the velocity distribution of the reference case (Fig. 12b, e, red lines) falls in between the velocity distributions of cases with heights 0.05 m (Fig. 12b, e, dashed blue line) and 0.1 m (Fig. 12b, e, dashed cyan line), while the water stage of the reference case (Fig. 12a, d, red line) is falling between the ranges of the same roughness cases (Fig. 12a, d, dashed blue and cyan lines). This indicates that the roughness height calibration with water stage is equivalent to calibrating it against water surface velocity. Noting that the water stage is highly sensitive to roughness at river banks, while the water surface velocity is more sensitive to roughness at the river thalweg, future model development may consider calibrating distinct roughness values for river

banks and thalwegs using a combined water-stage and surface velocity calibration.

4.1.4 Converted from Manning's coefficient

Though the above roughness calibration approach can be applied for any rivers where WSE observation is available, such a process is usually time consuming. 1-D and 2-D models have been widely used to predict WSE and Manning's coefficients have been available in these models. For example, for the river section studied in this work, the calibrated Manning coefficients from a 2-D CFD model, MASS2, are 0.038, 0.035, 0.034, 0.027, 0.027, and 0.03 (with units of $\mathrm{s\,m^{-1/3}}$) at 100B, 100N, 100D, LI, 100H, and 100F (Niehus et al., 2014). In these situations, the roughness parameter required in 3-D CFD models can be directly converted from the well-calibrated Manning coefficients based on a force balance at the riverbed. Specifically, the force balance can be described as $\tau_b = \rho g S R = 1/8 f \rho U^2$ with τ_b, S, R, f, and U denoting average bed shear stress, channel slope, hydraulic radius, Darcy–Weisbach friction factor, and average streamwise velocity. For gravel-bed rivers, it was shown that $\sqrt{\frac{8}{f}} = a(\frac{R}{k_s})^b$ with $b = 1/6$ and a has a value of 6.7, 7.3, 8.2, 8.4, 9.39, etc. when $R/k_s > 10$ (Chaudhry, 2008; Rickenmann and Recking, 2011; Ferguson, 2019). Meanwhile, the Manning equation shows $U = \frac{1}{n} R^{2/3} S^{1/2}$ with n denoting the Manning coefficient. Using these formulas, the relationship between n and k_s can be quantified as $n = \frac{1}{a\sqrt{g}} k_s^{1/6}$ if k_s has units of feet or $n = \frac{1.219}{a\sqrt{g}} k_s^{1/6}$ if k_s is in SI unit. The coefficient a characterizes the type of sediment that requires further calibration; however, it could use an average value of 8.0 for a rough estimation of k_s. In this work, as the locally optimal roughness height can be deterministically calculated and the modeled WSE at 100F gives a very good accuracy (see 100F in OF0 in Table 1), we back-calculated the value of $a = 8.4$ using $k_s = 7.42\,\mathrm{cm} = 0.2434\,\mathrm{ft}$ and $n = 0.03\,\mathrm{s\,m^{-1/3}}$. With the calibrated value for a, hydraulic roughness k_s can be converted as shown in case MS in Table 1. The modeling accuracy of WSE using these roughness parameters is -4.7–$7.7\,\mathrm{cm}$ and 6.4–$13.9\,\mathrm{cm}$ in terms of ME and MAE, respectively. This result suggests that the roughness height converted from the well-calibrated Manning coefficients of 2-D models can give similar modeling accuracy compared to using the globally optimal roughness height. Further local adjustment of these roughness parameters does not significantly improve modeling accuracy (see MS2 and MS3 in Table 1).

4.1.5 Estimated from microtopography

Both roughness calibration and conversion from the Manning coefficients require observation of the water stage and these calibrations may not guarantee the accuracy of other flow quantities such as bed shear stress and velocity. A more accurate and physics-based method for evaluating the effects of bed roughness is to directly resolve the influence of microtopography on flow dynamics. However, the success of such a method depends on high-resolution measurements of riverbed microtopography, computational techniques capable of resolving complex geometry in CFD codes, and available high-performance computing resources. Owing to the rapid development of structure-from-motion (SfM) photogrammetry and unnamed aerial vehicles, remote sensing of riverbed sediment structure with 1–5 cm resolution over a 40 km river reach has been possible for shallow streams (Carr et al., 2019). SfM survey of a patch-scale ($5\,\mathrm{m^2}$) natural streambed 0.5 m beneath water surface has also been recently realized with a 1 mm resolution (Danhoff and Huckins, 2020). These data can be used either for quantifying locally distributed grain size distribution or used as a geometric boundary for 3-D CFD models where the effects of sediment structure on flow dynamics can be directly resolved. At the patch scale (a few meters to tens meters), SfM photogrammetry-scanned high-resolution (mm- to cm-scale) natural riverbeds have been used to directly resolve the effects of sediment structure on the flow resistance (Chen et al., 2019). A quantitative relationship has been identified between hydraulic roughness height, turbulence vortex structure, and characteristic sediment size. Therefore, with available high-resolution riverbed structures from SfM and existing theories on hydraulic roughness, the distributed hydraulic roughness height in large rivers can be directly estimated and integrated with the CFD code.

4.2 OpenFOAM medium- and long-term water-stage prediction performance compared to 1-/2-D models

Though Sect. 4.1 discusses the roughness estimation procedure for a short time, we want to emphasize that the procedure and the usage of the roughness wall model are key to maintaining the model's accuracy over long time period and large spatial extent. Their importance can be illustrated by comparing the WSE from MASS1 (Richmond and Perkins, 2009), MASS2 (Niehus et al., 2014), OpenFOAM, and observations as shown in Fig. 13 and Table A3. Here, the three models are calibrated with WSE during similar time periods (October 2010–March 2011) using the same river topography, discharge, and stage data. The calibration accuracies of these three models are -0.2–$0.2\,\mathrm{cm}$, -3.8 to $-0.8\,\mathrm{cm}$ (Table A3), and -7.5–$6.4\,\mathrm{cm}$ (Table 1, case OF) in terms of ME, and 4.8–17.6 cm, 3.9–12.8 cm, and 7.5–12.7 cm in terms of MAE. These data demonstrate that the 1-D (MASS1) and 2-D (MASS2) models were calibrated to better accuracy than the 3-D model during the calibration period. Using this calibrated roughness, Fig. 13a compares the WSE from the three models and the observation at location 100B during April to June in 2013 (in the medium term). The result suggests that the 1-D and 2-D models overestimate the WSE of about 0.4 m, while the 3-D model is still very accurate for most dates, even though the 1-D/2-D models have a
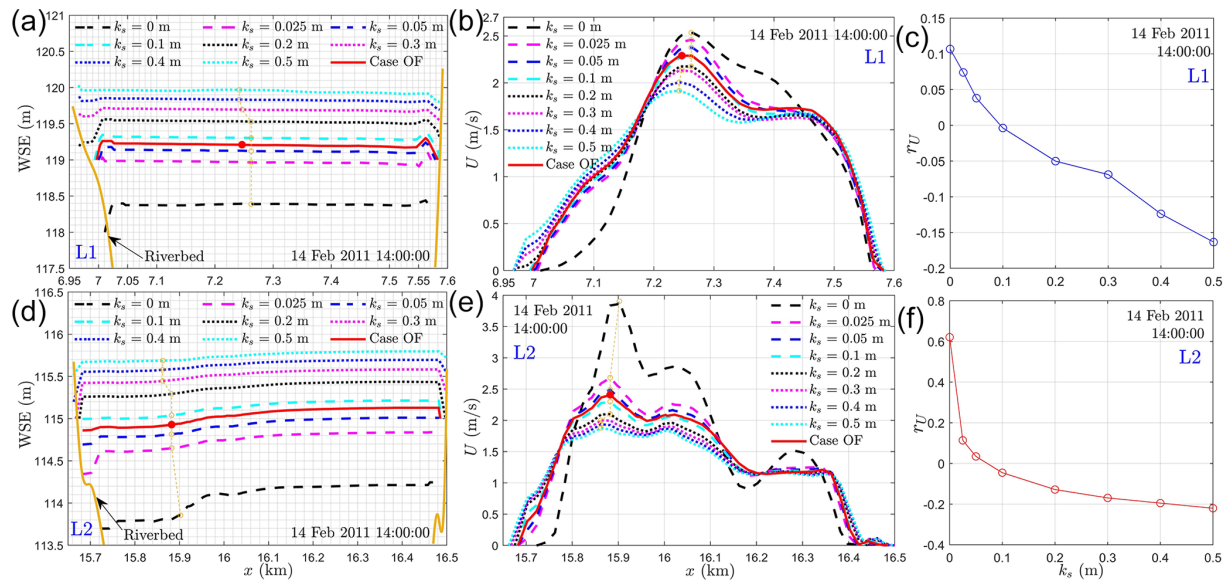
Figure 12. The spatial variations of water surface elevation **(a, d)** and free-surface velocity magnitude **(b, e)** under different roughness heights at transects L1 and L2 (see Fig. 1c) as well as the relative error **(c, f)** of the maximum free-surface velocity at each roughness height. Dashed circle lines and red dots in panels **(a)**–**(b)** and **(d)**–**(e)** denote the locations where the maximum velocity magnitude is reached. The r_U in panels **(c)**, **(f)** is defined as the relative velocity difference between the yellow circles and red dots in panels **(b)**, **(e)**.

better calibration accuracy. Further, to examine these models' long-term predictive capability at locations outside calibration locations, Fig. 13b compares the WSE from these models and another observation at location 100HD during 2018 and 2019 (long term). The result shows that the WSE predicted by the 1-D model deviates from that by the 2-D/3-D models and observations. Such a deviation can be more clearly observed through the 1 : 1 plot between modeled and observed WSE (Fig. 13c). Figure 13c also shows that the WSE from the MASS2 and OpenFOAM has no obvious bias relative to the observation data. Figure 13d further shows the 1 : 1 plot between modeled WSE from MASS1/MASS2 and OpenFOAM, which clearly suggests that WSE from MASS2 has similar a accuracy to OpenFOAM, but MASS1 deviates from it, especially at the lower WSE (low flow conditions). From these results, it is reasonable to conclude that the 3-D CFD model framework proposed in this work can reliably predict WSE over short-, medium-, and long-term periods at both calibration and non-calibration locations. The 1-D and 2-D models, though with accurate calibration, may not maintain its predictive capability for medium- and long-term streamflow at some locations. The lower accuracy of 1-D/2-D models may be attributed to their intrinsic physical simplifications, e.g., cross-sectional or depth average and resulting nonphysical meaning of roughness parameter (Lane et al., 2005; Lane and Ferguson, 2005), which necessitate recalibrating bed roughness to account for the dynamic changes in discharge.

4.3 Effects of discharge variations and topography heterogeneity on riverbed dynamic pressure

Riverbed dynamic pressure gradient affects the water exchange between the stream water and groundwater. Depending on the treatment of dynamic pressure, existing surface–subsurface interaction models can be categorized into three types: models without dynamic pressure, one-way coupled dynamic pressure models, and two-way coupled dynamic pressure models. The models that solve the surface water using 1-D/2-D Saint-Venant equations and 3-D hydrostatic Navier–Stokes equations belong to the first type because dynamic pressure is ignored (Maxwell et al., 2014). The second type solves the surface water using a 3-D hydrodynamic model and then uses the computed riverbed total pressure as a boundary condition for the subsurface flow without feeding the fluxes from the subsurface back to the surface water (Cardenas and Wilson, 2007; Bao et al., 2018; Zhou et al., 2018). The third type is similar to the second type but allows the fluxes from the subsurface back to surface water (Broecker et al., 2019; Li et al., 2020). Though the third type of model is desired to study the impact of dynamic pressure gradient on surface–subsurface interactions, it is currently limited to laboratory-scale and idealized flow conditions due to high computational costs and model instability. For the spatiotemporal scales studied in this work, the one-way coupled approach is the only solution. Despite the importance of the dynamic pressure, existing one-way coupled models usually neglect the effects of dynamic pressure based on an assumption that the dynamic pressure is negligible compared to the hy-
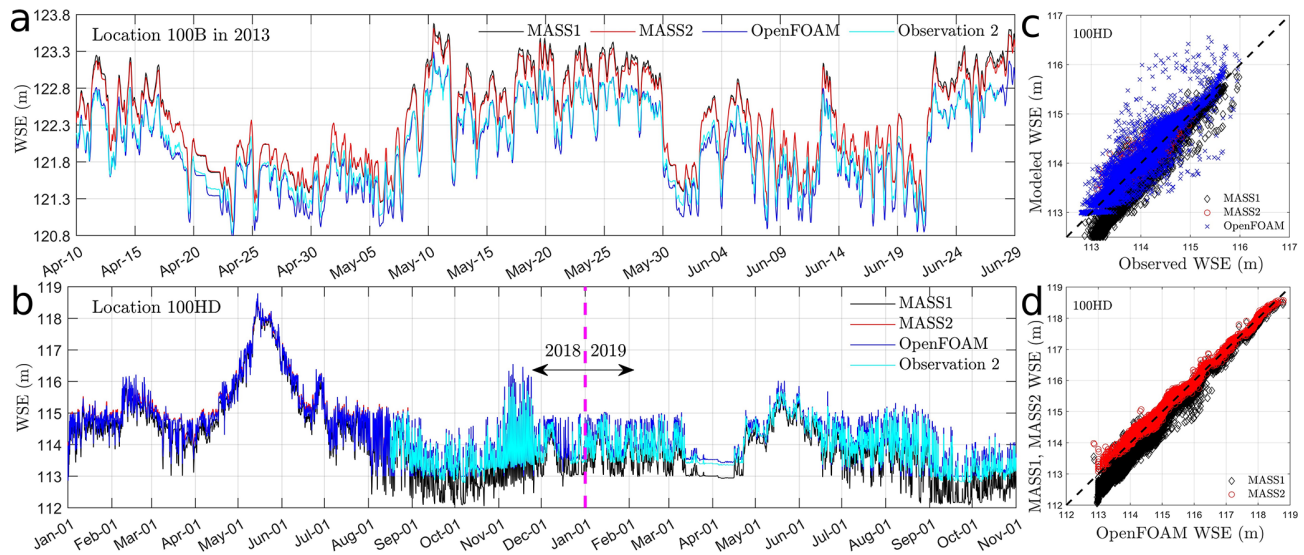
Figure 13. A comparison of water surface elevation (WSE) from MASS1, MASS2, OpenFOAM, and observations at 100B during 2013 **(a)** and at 100HD during 2018–2019 **(b)**. Panel **(c)** denotes the 1 : 1 plot of WSE between models and observation for 100HD, and **(d)** denotes that between OpenFOAM and MASS1/2. Details of the WSE from MASS1 and MASS2 can be found in Niehus et al. (2014).

drostatic pressure. With the CFD modeling results reported in Sect. 3.6, it is found that the relative importance of dynamic pressure to hydrostatic pressure varies with discharge and riverbed topography. In general, the dynamic pressure is less than 10 % of the hydrostatic pressure in 60 % to 80 % of the total wetted area and is between 10 % and 20 % of the hydrostatic pressure in 10 % to 30 % of the region. With variations in discharge, 20 % more area could be covered by higher dynamic pressure (10 % and 20 % of the hydrostatic pressure) at low flow ($< 2000 \, \mathrm{m^3 \, s^{-1}}$) compared to that at a high flow ($> 4000 \, \mathrm{m^3 \, s^{-1}}$). Spatially, both the main channel and dry–wet boundaries (shorelines and island boundaries) are likely covered with the above higher dynamic pressure at a low flow, while only the dry–wet boundaries are covered with the higher dynamic pressure at a high flow. As 30 % of the wetted area could be covered with dynamic pressure whose value is 10 % to 20 % of the hydrostatic pressure, whether it is acceptable to neglect the dynamic pressure in existing surface–subsurface models is questionable. In addition, the frequent discharge fluctuations cause variations in the magnitude and coverage area of the dynamic pressure. These dynamic variations likely further affect the water exchange rate between stream and groundwater. The specific impacts of riverbed dynamic pressure on the surface–subsurface exchange have been reported in another work of ours (Bao et al., 2022).

4.4 Computational efficiency

Despite the rapid growth in computational capacity in the past three decades, it is still a bottleneck for CFD modeling of natural rivers with tens of kilometers scale over mul-

tiple years. However, we show that such a limitation may be relieved using highly efficient CFD code, spatiotemporal decomposition approach, and a few hundred CPUs commonly available in university-scale or national-scale cyberinfrastructure. The discussion here is based on modeling results during 2011 (1 month), 2013–2015 (36 months), and 2018–2019 (22 months) by using Cascade, a high-performance computer managed by the Environmental Molecular Sciences Laboratory (EMSL) at PNNL (https://www.emsl.pnnl.gov, last access: 30 January 2022). For convenience, we define wall-clock time, CPU time, and solution time as the real-world time experienced by humans, the time consumed by the computer, and the time of water flow in the CFD model, respectively. With these definitions, the computational efficiency can be quantified by the ratio of solution time to wall-clock time.

Figure 14 shows the advancement of solution time with respect to wall-clock time for the short-term medium-flow case. It is observed that the computational efficiency, i.e., the slope of each line, increases linearly with increasing time step ΔT (solid lines with processor number $N_\mathrm{p} = 256$). In addition, increasing the number of processors from 256 to 512 only increases the computational efficiency by a factor of 1.5 (see magenta and cyan lines). Further increasing the number of processors decreases the computational efficiency, which means that an optimal number of processors, i.e., $N_\mathrm{p} = 512$, exists for our model. The computational efficiency is also affected by the selection of the linear solver. In our case, the PCG solver with DIC conditioner increases the computational efficiency by a factor of 3.6 compared to using a generalized geometric–algebraic multigrid (GAMG) solver (see blue and dashed black lines). Despite the changes
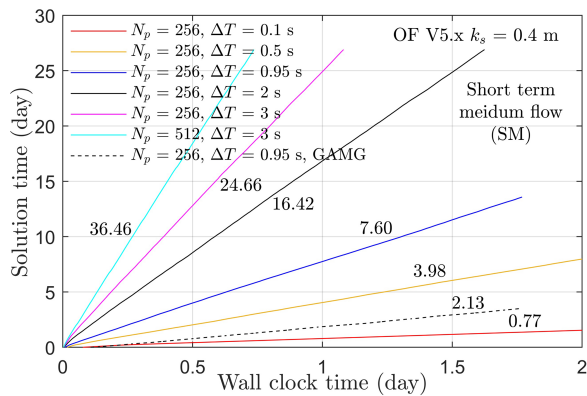
Figure 14. The advancement of solution time with respect to wall-clock time. N_p and ΔT denote the number of processors and time step. The linear solvers represented by solid and dashed lines are DIC-PCG and GAMG, respectively. The line slope or the computational efficiency is denoted by the values adjacent to each line.

in time step and number of processors, the modeled WSE does not change (see Fig. A4). Following these analyses, we show that the computational efficiency is around 36 by using 512 processors, 3 s as the time step, and DIC-PCG as the linear solver. This means we can simulate 1-month solution time in less than 1 d of wall-clock time or 1 d solution time in 40 min (1/36 d) of wall-clock time. With the same parallel computation setups, we divide simulations during medium term and long term into 36 and 22 cases and run all cases simultaneously. This approach does not reduce the total CPU time but significantly reduces the maximum wall-clock time required to complete all simulations. The OpenFOAM log files (see data sets) show that all simulations were completed in less than 6 d of wall-clock time. Considering the number of processors, the total CPU hours spent is about 1.1 million, which is equivalent to 19 000 CPU hours for each month. Note that the time considered here does not include the computational time used for calibration which is around 28 % of the total CPU hours. However, our work shows that calibration is only required once. Therefore, for rapid predictions of the streamflow with well-calibrated roughness parameters, the computational efficiency is likely feasible in terms of how much time and how many CPU hours are required.

5 Conclusions

This work proposed a semi-automated workflow that combines topographic and water-stage surveys, 3-D computational fluid dynamics modeling, a distributed rough wall resistance model, and spatiotemporal decomposition to simulate the streamflow in a 30 km long river reach in the Columbia River spanning 5 years. Specifically, a lidar-measured river topography is represented by a zig-zag grid in the 3-D model. The effect of geometric differences between an actual riverbed and the computational mesh on streamflow

is modeled with a distributed rough wall resistance model with the roughness parameters calibrated with measured WSE at six locations during 2011. The time decomposition approach enables decomposing the simulation period 2013–2015 into 36 months and 2018–2019 into 22 months with each month simulated simultaneously using parallel computation. Further computational efficiency analyses show that the time step, number of processors, and selection of linear solver affect the final computational efficiency. Using the spatiotemporal decomposition approach, the 3-D CFD modeling of the streamflow in 58 months can be achieved in less than 6 d with a cost of 1.1 million CPU hours.

Systematical roughness calibration shows that the distributed roughness field enables an average WSE difference between modeled and observed ones as −7.5–6.4 cm, which is equivalent to −2.7 %–2.1 % relative to average water depth. With this calibrated roughness field, the modeling accuracy for WSE is reported as −15.6–9.1 cm, −14.4 cm, and 7.2 cm for short-term, medium-term, and long-term predictions, which is equivalent to −7.1 %–6.6 %, −4.6 %, and 5.4 % relative to the average water depth. The model also demonstrates its predictive capability in reproducing the flow distribution and depth-averaged flow velocity at 9 out of 12 cross sections with correlation coefficients of 0.71–0.83. Using the validated modeling results, the relative importance of dynamic pressure to hydrostatic pressure and its dependencies on discharge variations and topography heterogeneity are further studied. It is found that the dynamic pressure is less than 10 % of the hydrostatic pressure in 60 % to 80 % of the total wetted area, while it is 10 % to 20 % of the hydrostatic pressure in 10 % to 30 % of the wetted region. The relative importance and the coverage area are found to change with discharge and locations.

Given the high modeling accuracy and computational efficiency of our model, this work provides a generic framework to evaluate and predict the impacts of climate- and human-induced discharge variations on river flow velocity, stage, and dynamic pressure at decadal temporal scales and tens-of-kilometers spatial scales that are relevant to the hyper-resolution (0.1–1 km) global- and continental-scale land surface (Wood et al., 2011; Bierkens et al., 2015) and groundwater modeling (Condon et al., 2021). With the discharge from global hydrological models at relevant scales, e.g., 5 to 10 km in space and hourly to daily in time (Lin et al., 2019; Alfieri et al., 2020; Harrigan et al., 2020; Yang et al., 2021), the streamflow model can be better constrained by climate- and human-induced discharge disturbances and can also serve as a test bed for the characterization of the processes at the scales (less than 0.1 km) not represented in global hydrologic models.

Appendix A: Uncertainty analyses

A1 Mesh resolution and time step uncertainty

The mesh resolution and time step are common sources of uncertainty of CFD models. As one goal of this paper is to predict the total pressure at the streambed, a summation of the hydrostatic pressure and the dynamic pressure, Fig. A1 shows the difference and the 1 : 1 plot of the total pressure head between a fine mesh (20 m × 20 m × 0.5 m) and a coarse mesh (20 m × 20 m × 1 m) at the time 16 PM 16 January 2013. The result shows that the difference is in the range −0.1–0.1 m at most of the locations and the spatial average difference is −0.03 m (Fig. A1a). The 1 : 1 plot also shows that the total pressure head from the two meshes almost overlaps with a mean difference, a root mean square, and a R^2 value as −0.03 m, 0.1 m, and 0.9987, respectively (Fig. A1b). Recalling that the WSE (related to the hydrostatic pressure head) observation itself could have an uncertainty of 0.032 m (see Appendix A2), the uncertainty attributed to mesh resolution is of a similar order of uncertainty in water-stage observation. This suggests that the mesh resolution does not contribute significant error to the total pressure head. To further evaluate the effect of time step, Fig. A4 shows a comparison of the modeled WSE using five different time steps at the six observation locations. The results reveal that the time step tested here does not affect the accuracy of WSE. Therefore, we choose the time step of 3 s as the final time step in order to reduce computational costs (see Sect. 2.7).

A2 Water-stage observation uncertainty

To illustrate the uncertainty in WSE observations, Fig. A7 shows a comparison of the WSE at 100B observed at two nearby locations. The results show that the ME between observation 2 and observation 1 is 3.219 cm; however, the standard deviation between the two observations is 11.555 cm (Fig. A7b). We argue that the large standard deviation is attributed to a small time uncertainty during the observation. This can be proven by Fig. A7c, which shows that the standard deviation reduces to 4.763 cm if the time history in observation 2 is shifted by 39.3 min. However, Fig. A7c also means the time shift does not contribute to a large uncertainty in its mean value as the ME is always in the range 3.08–3.22 cm for any time shift between −120 and 120 min. As the mean value of WSE is used to calibrate roughness, the above results thus demonstrate that the current WSE survey technique does not bring significant uncertainty for roughness quantification but could result in a large difference in standard deviation, mean absolute error, and root mean square when comparing the modeled WSE to observed ones. Actually, if we do an alignment of observation 2, i.e., shifting observation 2 by 39.3 min in time and adding 3.219 cm to its value, we see that the difference between observation 1 and such an aligned WSE is clearly reduced (Fig. A7b).
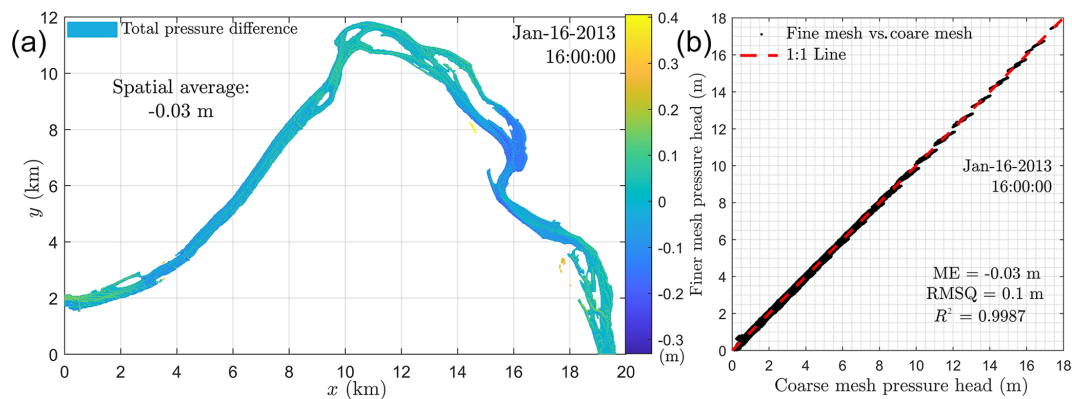

Figure A1. Distribution of the difference between total pressure modeled with a fine mesh and a coarse mesh **(a)**, and the 1 : 1 plot of the total pressure from the fine mesh and the coarse mesh **(b)**.
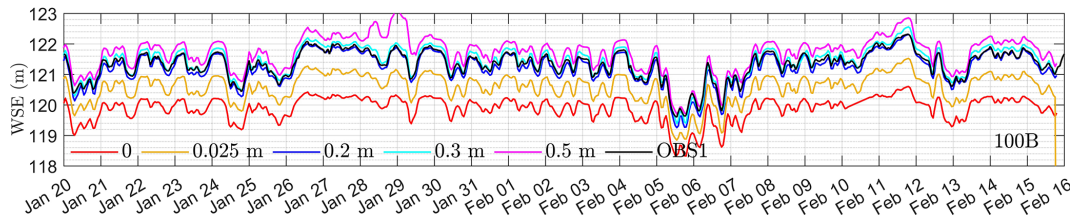
Figure A2. A comparison between observed WSE at 100B and modeled ones using different roughness heights.
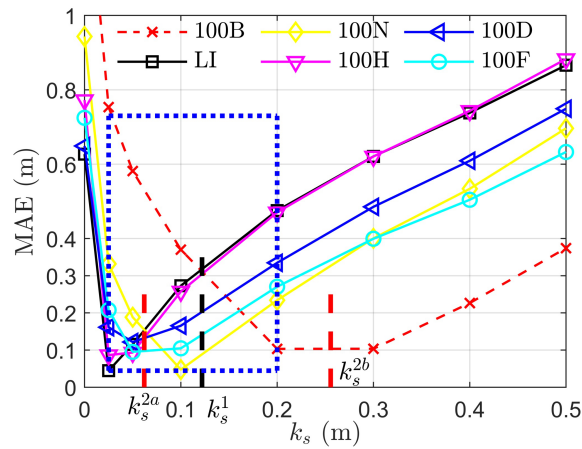

Figure A3. The variation of MAE between modeled and observed WSE at six locations using different roughness parameters. Black and red vertical lines represent the optimal roughness height using one-k_s and two-k_s strategies. Here, the one-k_s and two-k_s strategies represent using a single uniform or two uniform roughness heights for the streambed, respectively.
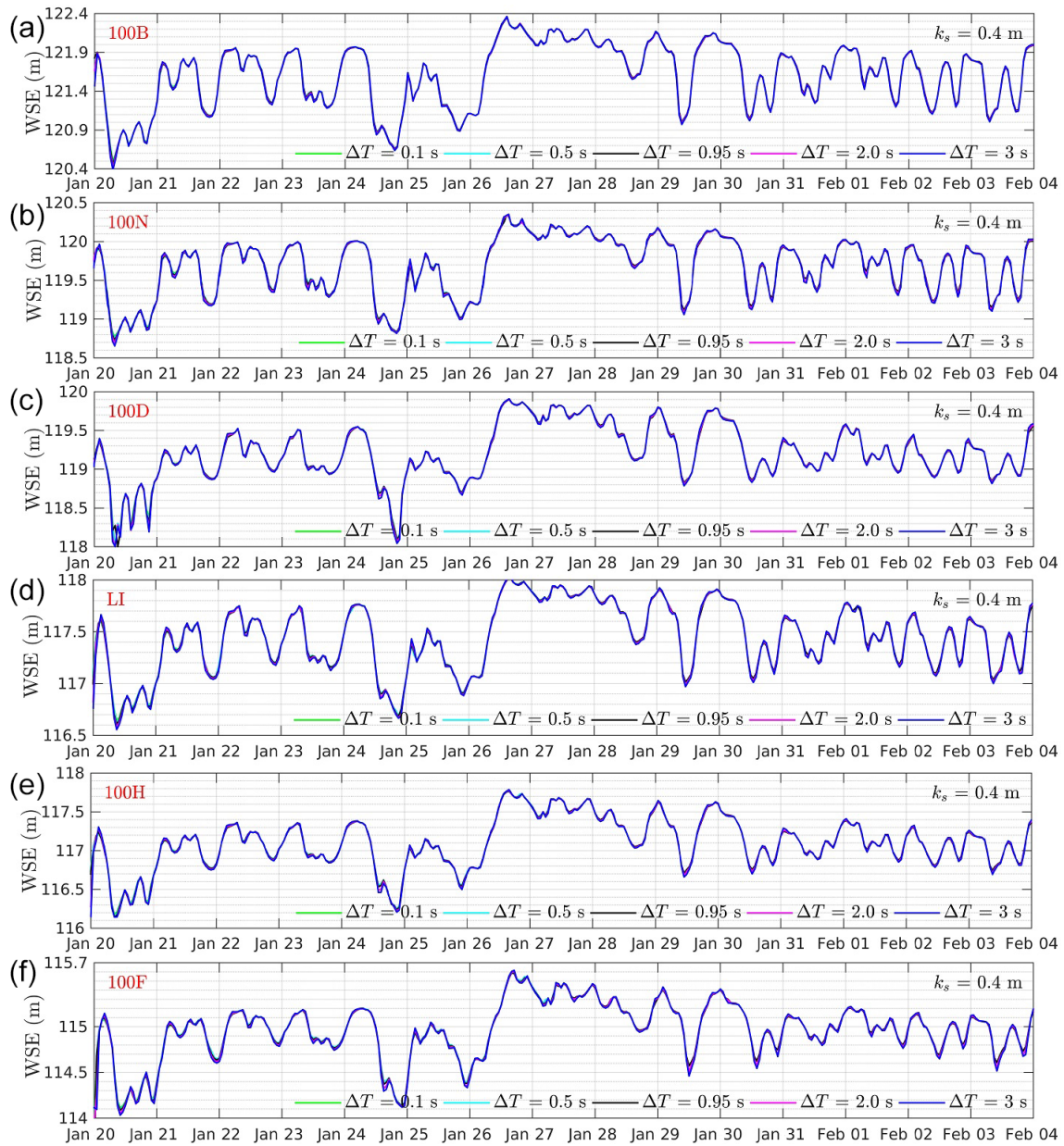
Figure A4. A comparison of WSE at different time steps at 100B, 100N, 100D, LI, 100H, and 100F.
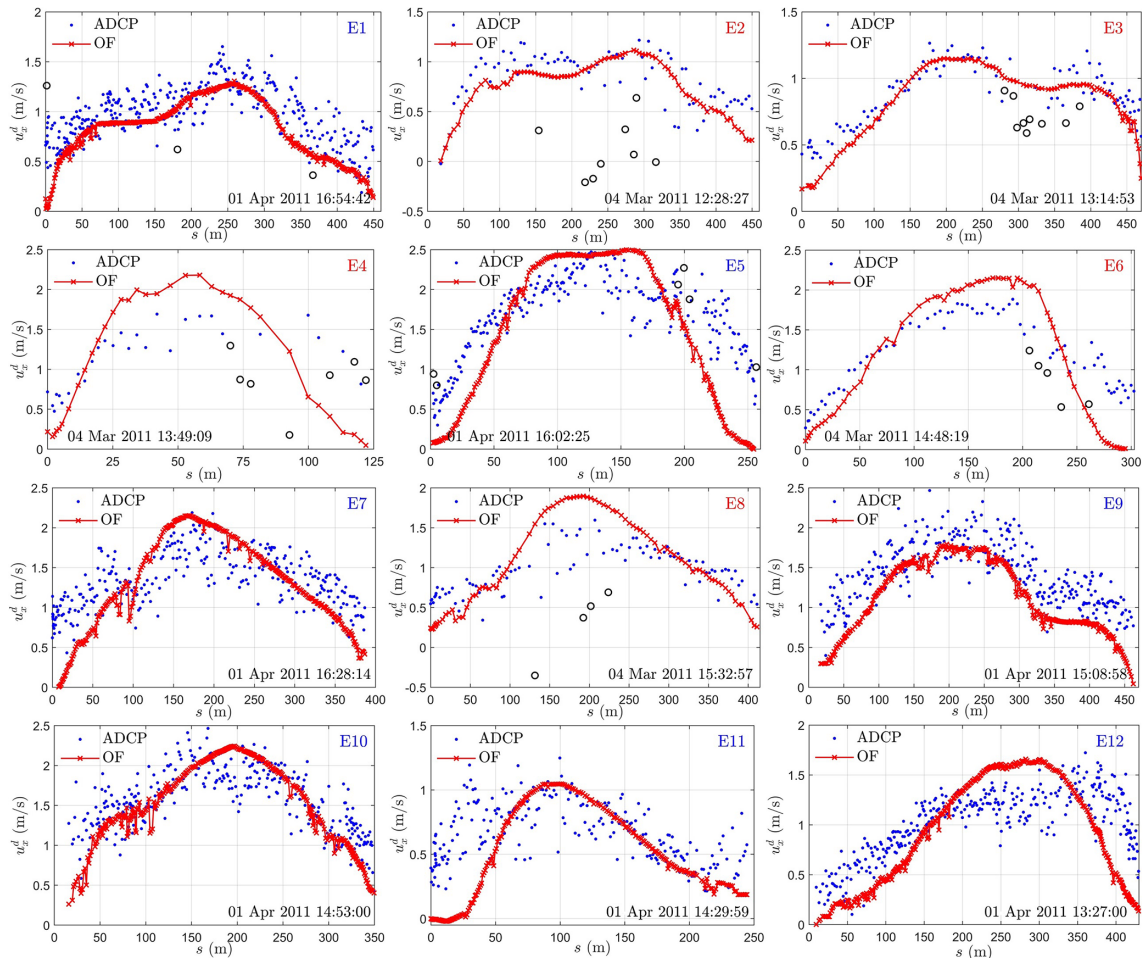
Figure A5. A comparison of depth-averaged velocity component along *x* from ADCP surveys and CFD modeling at E1–E12. Black circles denote measured outliers visually determined from Fig. A5 or Fig. A6.
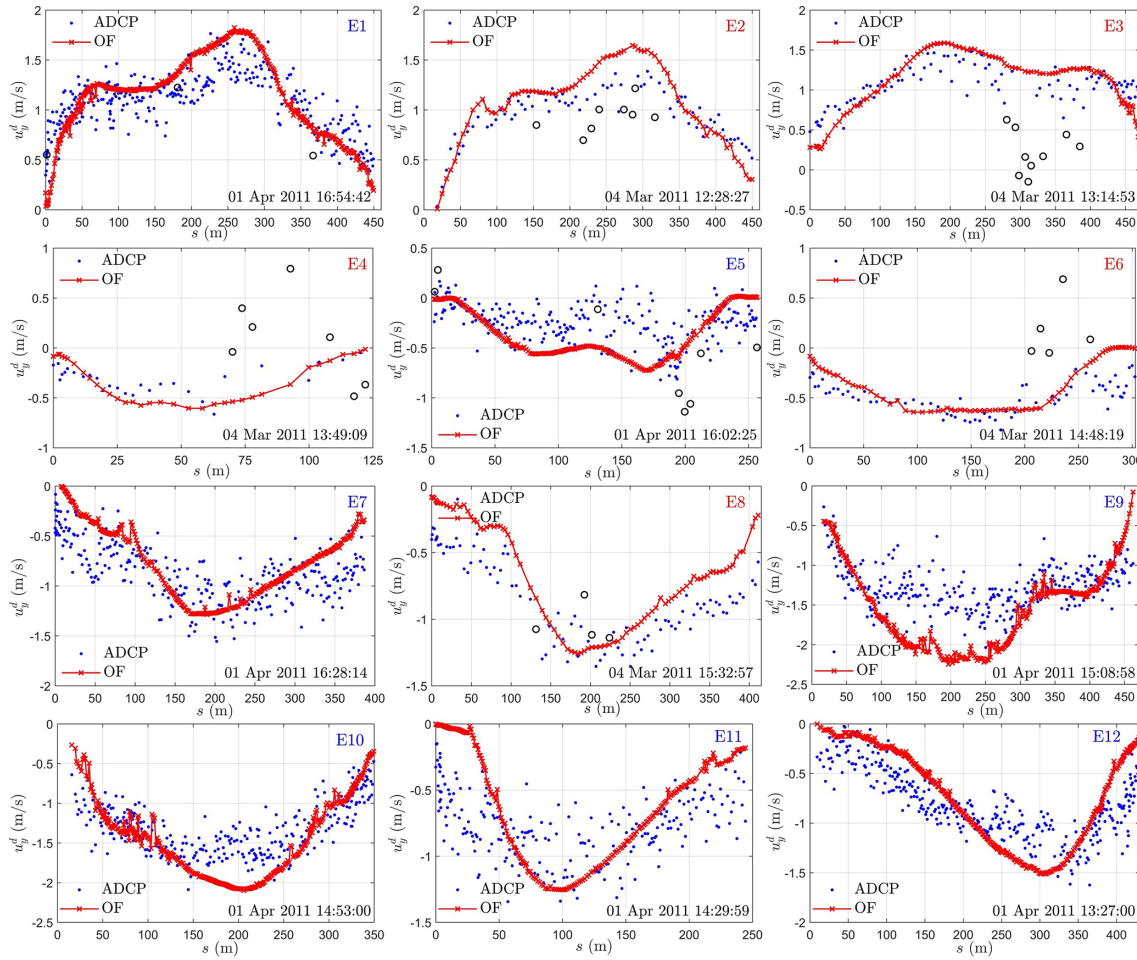
Figure A6. A comparison of depth-averaged velocity component along *y* from ADCP surveys and CFD modeling at E1–E12. Black circles denote measured outliers visually determined from Fig. A5 or Fig. A6.
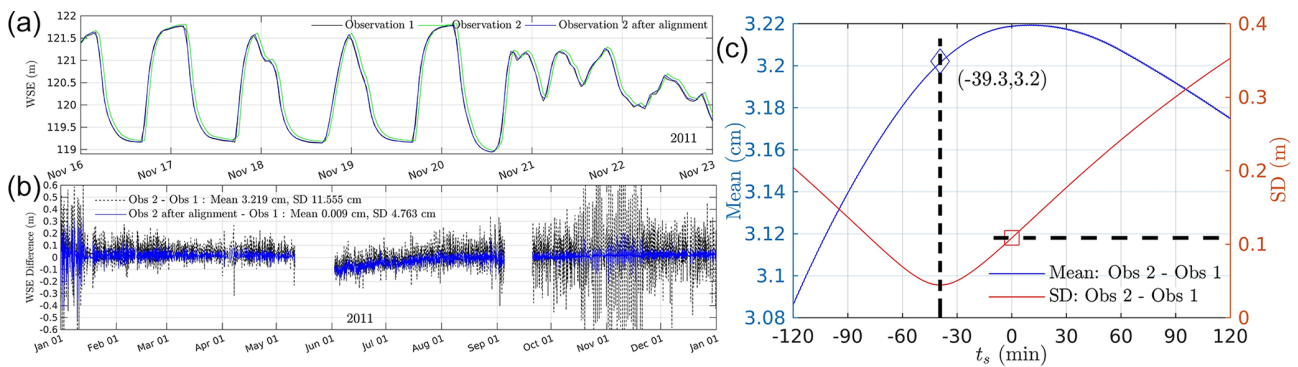
Figure A7. A comparison of WSE at 100B from observation 1, observation 2, and observation 2 after alignment (**a**), the differences in WSE between observation 1 and observation 2 and that between observation 1 and observation 2 after alignment (**b**), and the mean and standard deviation between observation 1 and observation 2 with a time shift t_s (**c**).
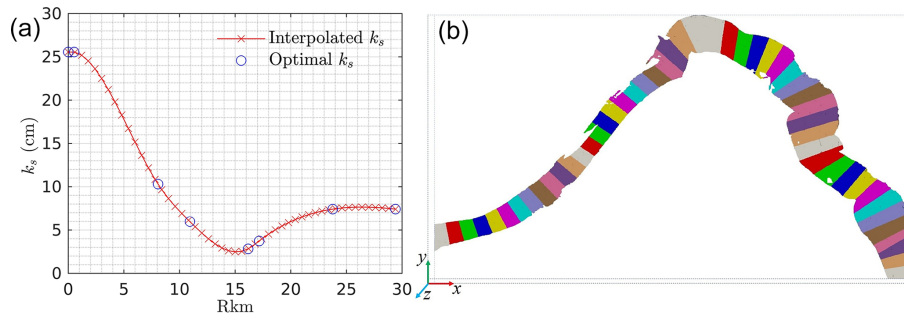
Figure A8. The roughness height on 50 pieces of stream interpolated from the six globally optimal roughness parameters (blue circle) **(a)** and the decomposition of the streambed into 50 pieces **(b)**.

Table A1. Horizontal coordinates and bed elevation of survey locations.

Station	x (m)	y (m)	z_b (m)
100B	555.63	1619.60	117.69
100N	6759.03	5882.76	116.26
100D	8516.19	8082.07	119.05
LI	12 580.24	10 298.23	113.74
100H	13 260.85	9756.13	114.45
100F	16 676.44	4429.60	110.77
100HD	15 451.55	7581.22	112.61

Table A2. Coefficients of the $k - \omega$ turbulence model.

β^*	$\alpha_{\omega 1}$	$\alpha_{\omega 2}$	α_{k1}	α_{k2}	β_1	β_2	γ_1	γ_1	a_1	b_1	c_1	C_μ
0.09	0.5	0.856	0.85	1	0.075	0.0828	0.555556	0.44	0.31	1	10	0.09

Table A3. Roughness parameters used in MASS1/2 and associated model accuracy.

Survey	MASS1 calibration				MASS1 validation		MASS2 calibration				MASS2 validation	
Station	n	k_s	ME	MAE	ME	MAE	n	k_s	ME	MAE	ME	MAE
100B	0.033	13.1	−0.2	17.6	24.0	26.0	0.038	30.5	−3.8	11.7	7.8	12.5
100N	0.0313	9.5	0.0	15.6	27.0	30.0	0.035	18.6	−2.8	12.8	4.5	8.4
100D	0.034	15.6	0.2	16.1	19.0	22.0	0.034	15.6	−2.7	10.2	3.3	4.7
LI	0.0346	17.3	0.1	4.8	NA	NA	0.027	3.9	−2.2	11.8	2.5	4.1
100H	0.0265	3.5	0.2	6.4	−1.0	4.9	0.027	3.9	−2.7	6.6	0.2	0.6
100F	0.0296	6.8	0.2	7.9	19.0	22.0	0.03	7.4	−0.8	3.9	1.9	3.9
Range	–	–	−0.2–0.2	4.8–17.6	−1.0–27.0	4.9–30.0	–	–	−3.8 to −0.8	3.9–12.8	0.2–7.8	0.6–12.5

Units for n, k_s, ME, and MAE are $\mathrm{s\,m^{-1/3}}$, cm, cm, and cm, respectively. The time periods for MASS1 calibration and validation is 3 October 2010–7 March 2011 and 1 July 2011–1 September 2011; and those for MASS2 are 4 October 2010–10 October 2010 and 4 January 2011–7 January 2011. Values of n, ME, and MAE can be found in Niehus et al. (2014). Values of k_s are used as a reference and calculated by $n = \frac{1.219}{a\sqrt{g}} k_s^{1/6}$ with $a = 8.4$ as discussed in Sect. 4.1.3.

Author contributions. YC contributed to the conceptualization, methodology, software, validation, analyses, investigation, and writing. JB contributed to the conceptualization, analyses, discussion, supervision, and project administration. YF contributed to the discussion. WAP contributed to the discussion and 1-D model data generation. HR contributed to the discussion, 1-D model data generation, and water-stage data preparation. XS contributed to the discussion. ZD contributed to geometry data preparation. ZH and XH contributed to the discussion. TDS contributed to project administration, funding acquisition, and discussion. All authors contributed to the paper review.

References

Alfieri, L., Lorini, V., Hirpa, F. A., Harrigan, S., Zsoter, E., Prudhomme, C., and Salamon, P.: A global stream-flow reanalysis for 1980–2018, J. Hydrol. X, 6, 100049, https://doi.org/10.1016/j.hydroa.2019.100049, 2020.

Bao, J., Zhou, T., Huang, M., Hou, Z., Perkins, W., Harding, S., Titzler, S., Hammond, G., Ren, H., Thorne, P., Suffield, S., Murray, C., and Zachara, J.: Modulating factors of hydrologic exchanges in a large-scale river reach: Insights from three-dimensional computational fluid dynamics simulations, Hydrol. Process., 32, 3446–3463, https://doi.org/10.1002/hyp.13266, 2018.

Bao, J., Chen, Y., Fang, Y., Song, X., Perkins, W., Duan, Z., Shuai, P., Ren, H., Hou, Z., Richmond, M., He, X., and Scheibe, T.: Modeling framework for evaluating the impacts of hydrodynamic pressure on hydrologic exchange fluxes and residence time for a large-scale river section over a long-term period, Environ. Modell. Softw., 148, 105277, https://doi.org/10.1016/j.envsoft.2021.105277, 2022.

Bates, P. D., Anderson, M. G., and Hervouet, J. M.: Initial comparison of two two-dimensional finite element codes for river flood simulation, P. I. Civil Eng.-Water, 112, 238–248, https://doi.org/10.1680/iwtme.1995.27886, 1995.

Bates, P. D., Lane, S. N., and Ferguson, R. I.: Computational fluid dynamics: applications in environmental hydraulics, edited by: Bates, P. D., Lane, S. N., and Ferguson, R. I., John Wiley & Sons, Ltd, Chichester, UK, https://doi.org/10.1002/0470015195, 2005.

Berenbrock, C. and Tranmer, A. W.: Simulation of flow, sediment transport, and sediment mobility of the Lower Coeur d'Alene River, Idaho, USGS Scientific Investigations Report, p. 164, https://doi.org/10.3133/sir20085093, 2008.

Biddanda, B. A.: Global significance of the changing freshwater carbon cycle, EOS, 98, 6, 15–17, https://doi.org/10.1029/2017EO069751, 2017

Bierkens, M. F. P., Bell, V. A., Burek, P., Chaney, N., Condon, L. E., David, C. H., de Roo, A., Döll, P., Drost, N., Famiglietti, J. S., Flörke, M., Gochis, D. J., Houser, P., Hut, R., Keune, J., Kollet, S., Maxwell, R. M., Reager, J. T., Samaniego, L., Sudicky, E., Sutanudjaja, E. H., van de Giesen, N., Winsemius, H., and Wood, E. F.: Hyper-resolution global hydrological modelling: what is next?, Hydrol. Process., 29, 310–320, https://doi.org/10.1002/hyp.10391, 2015.

Blocken, B., Stathopoulos, T., and Carmeliet, J.: CFD simulation of the atmospheric boundary layer: wall function problems, Atmos. Environ., 41, 238–252, https://doi.org/10.1016/j.atmosenv.2006.08.019, 2007.

Blumberg, A. F. and Mellor, G. L.: Diagnostic and prognostic numerical circulation studies of the South Atlantic Bight, J. Geophys. Res.-Oceans, 88, 4579–4592, https://doi.org/10.1029/JC088iC08p04579, 1983.

Booker, D. J., Sear, D. A., and Payne, A. J.: Modelling three-dimensional flow structures and patterns of boundary shear stress in a natural pool-riffle sequence, Earth Surf. Proc. Land., 26, 553–576, https://doi.org/10.1002/esp.210, 2001.

Bovee, K. D.: The incremental method of assessing habitat potential for coolwater species, with management implications, in: American Fisheries Society Special Publication, 1st edn., vol. 11, edited by: Kendall, R. L., Amer Fisheries Society, pp. 340–346, ISBN-10 0913235083, ISBN-13 978-0913235089, 1978.

Broecker, T., Teuber, K., Sobhi Gollo, V., Nützmann, G., Lewandowski, J., and Hinkelmann, R.: Integral flow modelling approach for surface water-groundwater interactions along a rippled streambed, Water, 11, 1517, https://doi.org/10.3390/w11071517, 2019.

Cao, Z., Carling, P., and Oakey, R.: Flow reversal over a natural pool-riffle sequence: a computational study, Earth Surf. Proc. Land., 28, 689–705, https://doi.org/10.1002/esp.466, 2003.

Cardenas, M. B. and Wilson, J. L.: Dunes, turbulent eddies, and interfacial exchange with permeable sediments, Water Resour.

Res., 43, W08412, https://doi.org/10.1029/2006WR005787, 2007.

Carling, P. A. and Wood, N.: Simulation of flow over pool-riffle topography: a consideration of the velocity reversal hypothesis, Earth Surf. Proc. Land., 19, 319–332, https://doi.org/10.1002/esp.3290190404, 1994.

Carr, J. C., DiBiase, R. A., and Yeh, E. C.: Geomorphic and structural mapping for remote bedrock river corridors in the Taiwan Central Range using paired outcrop and kilometer scale UAV surveys, in: GSA Annual Meeting, Phoenix, Arizona, USA, 22–25 September 2019,https://doi.org/10.1130/abs/2019AM-335826, 2019.

CFDDirect: OpenFOAM-5.x: free open source CFD, http://www.OpenFoam.org (last access: 30 January 2022), 2017.

Chaudhry, M. H. H. (Ed.): Open-channel flow, Springer US, New York, NY, USA, 2nd edn., https://doi.org/10.1007/978-0-387-68648-6, 2008.

Chen, Y., Dibiase, R. A. R. A., McCarroll, N., and Liu, X.: Quantifying flow resistance in mountain streams using computational fluid dynamics modeling over structure-from-motion photogrammetry-derived microtopography, Earth Surf. Proc. Land., 44, 1973–1987, https://doi.org/10.1002/esp.4624, 2019.

Chen, Y., Bao J., Fang, Y., Perkings, W. A., Ren, H., Song, X., Duan, Z., Hou, Z., He, X., Scheibe, T. D.: (2021): Model, data, and code for paper "Modeling of streamflow in a 30-kilometer-long reach spanning 5 years using OpenFOAM 5.x", River Corridor and Watershed Biogeochemistry SFA, ESS-DIVE repository [data set, code], https://doi.org/10.15485/1819956, 2021.

Condon, L. E., Kollet, S., Bierkens, M. F. P., Fogg, G. E., Maxwell, R. M., Hill, M. C., Fransen, H. H., Verhoef, A., Van Loon, A. F., Sulis, M., and Abesser, C.: Global Groundwater Modeling and Monitoring: Opportunities and Challenges, Water Resour. Res., 57, e2020WR029500, https://doi.org/10.1029/2020WR029500, 2021.

Correia, L. P., Krishnappan, B. G., and Graf, W. H.: Fully coupled unsteady mobile boundary flow model, J. Hydraul. Eng., 118, 476–494, https://doi.org/10.1061/(ASCE)0733-9429(1992)118:3(476), 1992.

Crowder, D. W. and Diplas, P.: Evaluating spatially explicit metrics of stream energy gradients using hydrodynamic model simulations, Can. J. Fish. Aquat. Sci., 57, 1497–1507, https://doi.org/10.1139/f00-074, 2000.

Cui, Y., Parker, G., Pizzuto, J., and Lisle, T. E.: Sediment pulses in mountain rivers: 2. comparison between experiments and numerical predictions, Water Resour. Res., 39, 1240, https://doi.org/10.1029/2002WR001805, 2003.

Danhoff, B. M. and Huckins, C. J.: Modelling submerged fluvial substrates with structure-from-motion photogrammetry, River Res. Appl., 36, 128–137, https://doi.org/10.1002/rra.3532, 2020.

Darby, S. E., Alabyan, A. M., and Van de Wiel, M. J.: Numerical simulation of bank erosion and channel migration in meandering rivers, Water Resour. Res., 38, 1163, https://doi.org/10.1029/2001WR000602, 2002.

Demuren, A. O.: A numerical model for flow in meandering channels with natural bed topography, Water Resour. Res., 29, 1269–1277, https://doi.org/10.1029/92WR02907, 1993.

Demuren, A. O. and Rodi, W.: Calculation of flow and pollutant dispersion in meandering channels, J. Fluid Mech., 172, 63–92, https://doi.org/10.1017/S0022112086001659, 1986.

Deshpande, S. S., Anumolu, L., and Trujillo, M. F.: Evaluating the performance of the two-phase flow solver interFoam, Computational Science & Discovery, 5, 14016, https://doi.org/10.1088/1749-4699/5/1/014016, 2012.

Duan, J. G., Wang, S. S. Y., and Jia, Y.: The applications of the enhanced CCHE2D model to study the alluvial channel migration processes, J. Hydraul. Res., 39, 469–480, https://doi.org/10.1080/00221686.2001.9628272, 2001.

Ferguson, R. I.: Reach-Scale Flow Resistance, in: Treatise on Geomorphology, second edn., vol. 6, edited by: Shroder, J. F., Academic Press, 110–132, ISBN 978-0-12-818235-2, https://doi.org/10.1016/B978-0-12-409548-9.09386-6, 2022.

Ferguson, R. I., Church, M., and Weatherly, H.: Fluvial aggradation in Vedder River: testing a one-dimensional sedimentation model, Water Resour. Res., 37, 3331–3347, https://doi.org/10.1029/2001WR000225, 2001.

Hamrick, J. M.: A three-dimensional environmental fluid dynamics computer code: theoretical and computational aspects, in: Special report in applied marine science and ocean engineering, 317, p. 64, Virginia Institute of Marine Science, College of William and Mary, https://doi.org/10.21220/V5TT6C, 1992.

Hardy, R. J. J., Lane, S. N. N., Lawless, M. R. R., Best, J. L. L., Elliott, L., and Ingham, D. B. B.: Development and testing of a numerical code for treatment of complex river channel topography in three-dimensional CFD models with structured grids, J. Hydraul. Res., 43, 468–480, https://doi.org/10.1080/00221680509500145, 2005.

Harrigan, S., Zsoter, E., Alfieri, L., Prudhomme, C., Salamon, P., Wetterhall, F., Barnard, C., Cloke, H., and Pappenberger, F.: GloFAS-ERA5 operational global river discharge reanalysis 1979–present, Earth Syst. Sci. Data, 12, 2043–2060, https://doi.org/10.5194/essd-12-2043-2020, 2020.

Harvey, J. W.: Hydrologic Exchange Flows and Their Ecological Consequences in River Corridors, in: Stream Ecosystems in a Changing Environment, edited by: Jones, J. B. and Stanley, E. H., Academic Press, 1–83, ISBN 978-0-12-405890-3, https://doi.org/10.1016/B978-0-12-405890-3.00001-4, 2016.

Hester, E. T., Cardenas, M. B., Haggerty, R., and Apte, S. V.: The importance and challenge of hyporheic mixing, Water Resour. Res., 53, 3565–3575, https://doi.org/10.1002/2016WR020005, 2017.

Hicks, F. E. and Peacock, T.: Suitability of HEC-RAS for flood forecasting, Can. Water Resour. J., 30, 159–174, https://doi.org/10.4296/cwrj3002159, 2005.

Hiemstra, K. S., van Vuren, S., Vinke, F. S. R., Jorissen, R. E., and Kok, M.: Assessment of the functional performance of lowland river systems subjected to climate change and large-scale morphological trends, International Journal of River Basin Management, 20, 45–56, https://doi.org/10.1080/15715124.2020.1790580, 2020.

Hirt, C. W. and Nichols, B. D.: Volume of fluid (VOF) method for the dynamics of free boundaries, J. Computat. Phys., 39, 201–225, https://doi.org/10.1016/0021-9991(81)90145-5, 1981.

Hodskinson, A.: Computational fluid dynamics as a tool for investigating separated flow in river bends, Earth Surf. Proc. Land., 21, 993–1000, https://doi.org/10.1002/(SICI)1096-9837(199611)21:11<993::AID-ESP698>3.0.CO;2-R, 1996.

Hodskinson, A. and Ferguson, R. I.: Numerical modelling of separated flow in river bends: model testing and ex-

perimental investigation of geometric controls on the extent of flow separation at the concave bank, Hydrol. Process., 12, 1323–1338, https://doi.org/10.1002/(SICI)1099-1085(19980630)12:8<1323::AID-HYP617>3.0.CO;2-S, 1998.

Hoey, T. B. and Ferguson, R.: Numerical simulation of downstream fining by selective transport in gravel bed rivers: model development and illustration, Water Resour. Res., 30, 2251–2260, https://doi.org/10.1029/94WR00556, 1994.

Horritt, M. S.: Parameterisation, validation and uncertainty analysis of CFD models of fluvial and flood hydraulics in the natural environment, in: Computational Fluid Dynamics, edited by: Bates, P. D., Lane, S. N., and Ferguson, R. I., pp. 193–213, John Wiley & Sons, Ltd, Chichester, UK, https://doi.org/10.1002/0470015195.ch9, 2005.

Howard, A. D.: Modeling channel migration and floodplain sedimentation in meandering streams, in: Lowland floodplain rivers : geomorphological perspectives, edited by: Carling, P. A. and Petts, G. E., p. 302, John Wiley, Chichester, UK, ISBN-10 0471931195, ISBN-13 978-0471931195, 1992.

Huang, J., Patel, V. C., Lai, Y. G., and Weber, L. J.: Simulation study of flow through a reach of the Chattachoochee River, J. Hydraul. Res., 42, 487–492, https://doi.org/10.1080/00221686.2004.9641218, 2004.

Issa, R. I.: Solution of the implicitly discretised fluid flow equations by operator-splitting, J. Comput. Phys., 62, 40–65, https://doi.org/10.1016/0021-9991(86)90099-9, 1985.

Ji, Z., Hu, G., Shen, J., and Wan, Y.: Three-dimensional modeling of hydrodynamic processes in the St. Lucie Estuary, Estuarine, Coastal and Shelf Science, 73, 188–200, https://doi.org/10.1016/j.ecss.2006.12.016, 2007.

Johnson, B. H., Kim, K. W., Heath, R. E., Hsieh, B. B., and Butler, H. L.: Validation of three-dimensional hydrodynamic model of Chesapeake Bay, J. Hydraul. Eng., 119, 2–20, https://doi.org/10.1061/(ASCE)0733-9429(1993)119:1(2), 1993.

Kang, S. and Sotiropoulos, F.: Flow phenomena and mechanisms in a field-scale experimental meandering channel with a pool-riffle sequence: Insights gained via numerical simulation, J. Geophys. Res., 116, F03011, https://doi.org/10.1029/2010JF001814, 2011.

Kang, S. and Sotiropoulos, F.: Assessing the predictive capabilities of isotropic, eddy viscosity Reynolds-averaged turbulence models in a natural-like meandering channel, Water Resour. Res., 48, W06505, https://doi.org/10.1029/2011WR011375, 2012.

Kang, S., Lightbody, A., Hill, C., and Sotiropoulos, F.: High-resolution numerical simulation of turbulence in natural waterways, Adv. Water Resour., 34, 98–113, https://doi.org/10.1016/j.advwatres.2010.09.018, 2011.

Keller, E. A. and Florsheim, J. L.: Velocity-reversal hypothesis: a model approach, Earth Surf. Proc. Land., 18, 733–740, https://doi.org/10.1002/esp.3290180807, 1993.

Khosronejad, A., Le, T., DeWall, P., Bartelt, N., Woldeamlak, S., Yang, X., and Sotiropoulos, F.: High-fidelity numerical modeling of the Upper Mississippi River under extreme flood condition, Adv. Water Resour., 98, 97–113, https://doi.org/10.1016/j.advwatres.2016.10.018, 2016.

Khosronejad, A., Flora, K., and Kang, S.: Effect of inlet turbulent boundary conditions on scour predictions of coupled LES and morphodynamics in a field-scale river:

bankfull flow conditions, J. Hydraul. Eng., 146, 04020020, https://doi.org/10.1061/(ASCE)HY.1943-7900.0001719, 2020.

Kolden, E., Fox, B. D., Bledsoe, B. P., and Kondratieff, M. C.: Modelling whitewater park hydraulics and fish habitat in Colorado, River Res. Appl., 32, 1116–1127, https://doi.org/10.1002/rra.2931, 2016.

Kuzmin, D., Möller, M., and Turek, S.: Multidimensional FEM-FCT schemes for arbitrary time stepping, Int. J. Numer. Meth. Fl., 42, 265–295, https://doi.org/10.1002/fld.493, 2003.

Lai, Y. G.: Quantitative modeling tools for large wood debris and other in-stream structures, Tech. Rep. ST-2016-4495-01, U.S. Department of the Interior, Bureau of Reclamation, Denver, CO, https://www.usbr.gov/research/projects/download_product.cfm?id=938 (last access: 4 April 2022), 2016.

Lane, S. N. and Ferguson, R. I.: Modelling reach-scale fluvial flows, in: Computational Fluid Dynamics, edited by: Bates, P. D., Lane, S. N., and Ferguson, R. I., pp. 215–269, John Wiley & Sons, Ltd, Chichester, UK, https://doi.org/10.1002/0470015195.ch10, 2005.

Lane, S. N. and Richards, K. S.: High resolution, two-dimensional spatial modelling of flow processes in a multi-thread channel, Hydrol. Process., 12, 1279–1298, https://doi.org/10.1002/(SICI)1099-1085(19980630)12:8<1279::AID-HYP615>3.0.CO;2-E, 1998.

Lane, S. N., Bradbrook, K. F., Richards, K. S., Biron, P. A., and Roy, A. G.: The application of computational fluid dynamics to natural river channels: three-dimensional versus two-dimensional approaches, Geomorphology, 29, 1–20, https://doi.org/10.1016/S0169-555X(99)00003-3, 1999.

Lane, S. N., Hardy, R. J., Elliot, L., Ingham, D. B., Elliott, L., Ingham, D. B., Elliot, L., and Ingham, D. B.: Numerical modeling of flow processes over gravelly surfaces using structured grids and a numerical porosity treatment, Water Resour. Res., 40, W01302, https://doi.org/10.1029/2002WR001934, 2004.

Lane, S. N., Hardy, R. J., Ferguson, R. I., and Parsons, D. R.: A framework for model verification and validation of CFD schemes in natural open channel flows, in: Computational Fluid Dynamics, edited by: Bates, P. D., Lane, S. N., and Ferguson, R. I., pp. 169–192, John Wiley & Sons, Ltd, Chichester, UK, https://doi.org/10.1002/0470015195.ch8, 2005.

Le, T. B., Khosronejad, A., Sotiropoulos, F., Bartelt, N., Woldeamlak, S., and Dewall, P.: Large-eddy simulation of the Mississippi River under base-flow condition: hydrodynamics of a natural diffluence-confluence region, J. Hydraul. Res., 57, 836–851, https://doi.org/10.1080/00221686.2018.1534282, 2019.

Leclerc, M., Boudreault, A., Bechara, T. A., and Corfa, G.: Two-dimensional hydrodynamic modeling: a neglected tool in the instream flow incremental methodology, T. Am. Fish. Soc., 124, 645–662, https://doi.org/10.1577/1548-8659(1995)124<0645:TDHMAN>2.3.CO;2, 1995.

Leschziner, M. A. and Rodi, W.: Calculation of strongly curved open channel flow, J. Hydraul. Eng. Div., 105, 1297–1314, https://doi.org/10.1061/JYCEAJ.0005286, 1979.

Lesser, G. R., Roelvink, J. A., van Kester, J. A. T. M., and Stelling, G. S.: Development and validation of a three-dimensional morphological model, Coast. Eng., 51, 883–915, https://doi.org/10.1016/j.coastaleng.2004.07.014, 2004.

Li, B., Liu, X., Kaufman, M. H., Turetcaia, A., Chen, X., and Cardenas, M. B.: Flexible and modular simultaneous

modeling of flow and reactive transport in rivers and hyporheic zones, Water Resour. Res., 56, e2019WR02652, https://doi.org/10.1029/2019WR026528, 2020.

Lin, P., Pan, M., Beck, H. E., Yang, Y., Yamazaki, D., Frasson, R., David, C. H., Durand, M., Pavelsky, T. M., Allen, G. H., Gleason, C. J., and Wood, E. F.: Global Reconstruction of Naturalized River Flows at 2.94 Million Reaches, Water Resour. Res., 55, 6499–6516, https://doi.org/10.1029/2019WR025287, 2019.

Liu, X., Chen, Y., and Shen, C.: Coupled two-dimensional surface flow and three-dimensional sub-surface flow modeling for the drainage of permeable road pavement, J. Hydrol. Eng., 21, 4016051, https://doi.org/10.1061/(ASCE)HE.1943-5584.0001462, 2016.

Lorke, A. and MacIntyre, S.: The benthic boundary layer (in rivers, lakes, and reservoirs), in: Encyclopedia of Inland Waters, edited by: Likens, G. E., pp. 505–514, Elsevier, https://doi.org/10.1016/B978-012370626-3.00079-X, 2009.

Ma, L., Ashworth, P. J., Best, J. L., Elliott, L., Ingham, D. B., and Whitcombe, L. J.: Computational fluid dynamics and the physical modelling of an upland urban river, Geomorphology, 44, 375–391, https://doi.org/10.1016/S0169-555X(01)00184-2, 2002.

Marjoribanks, T. I., Hardy, R. J., Lane, S. N., and Tancock, M. J.: Patch-scale representation of vegetation within hydraulic models, Earth Surf. Proc. Land., 42, 699–710, https://doi.org/10.1002/esp.4015, 2017.

Maxwell, R. M., Putti, M., Meyerhoff, S., Delfs, J.-O., Ferguson, I. M., Ivanov, V., Kim, J., Kolditz, O., Kollet, S. J., Kumar, M., Lopez, S., Niu, J., Paniconi, C., Park, Y.-J., Phanikumar, M. S., Shen, C., Sudicky, E. A., and Sulis, M.: Surface-subsurface model intercomparison: A first set of benchmark results to diagnose integrated hydrology and feedbacks, Water Resour. Res., 50, 1531–1549, https://doi.org/10.1002/2013WR013725, 2014.

Menter, F. R., Kuntz, M., and Langtry, R.: Ten years of industrial experience with the SST turbulence model turbulence heat and mass transfer, in: Proceedings of the 4th International Symposium on Turbulence, Heat and Mass Transfer, edited by: Hanjalic, K., Nagano, Y., and Tummers, M. J., pp. 625–632, Begell House, Antalya, Turkey, http://citeseerx.ist.psu.edu/viewdoc/download?doi=10.1.1.460.2814&rep=rep1&type=pdf (last access: 4 April 2022), 2003.

Milhous, R. T., Wegner, D. L., and Waddle, T.: User's guide to the physical habitat simulation system (PHABISM), in: FWS/OBS, 81/43, p. FWS/OBS, U.S. Fish and Wildlife Service, https://pubs.er.usgs.gov/publication/fwsobs81_43 (last access: 4 April 2022), 1984.

Miller, A. J.: Debris-fan constrictions and flood hydraulics in river canyons: Some implications from two-dimensional flow modelling, Earth Surf. Proc. Land., 19, 681–697, https://doi.org/10.1002/esp.3290190803, 1994.

Nagata, N., Hosoda, T., and Muramoto, Y.: Numerical analysis of river channel processes with bank erosion, J. Hydraul. Eng., 126, 243–252, https://doi.org/10.1061/(ASCE)0733-9429(2000)126:4(243), 2000.

Nicholas, A. P. and Sambrook Smith, G. H.: Numerical simulation of three-dimensional flow hydraulics in a braided channel, Hydrol. Process., 13, 913–929, https://doi.org/10.1002/(SICI)1099-1085(19990430)13:6<913::AID-HYP764>3.0.CO;2-N, 1999.

Niehus, S., Perkins, W., and Richmond, M.: Simulation of Columbia River Hydrodynamics and Water Temperature from

1917 through 2011 in the Hanford Reach, Tech. Rep. PNWD-3278, Battelle-Pacific Northwest Division, Richland, WA, https://doi.org/10.13140/RG.2.1.5146.8409, 2014.

Nikuradse, J.: Laws of flow in rough pipes (English translation), Tech. Rep., National Advisory Commission for Aeronautics, Washington, DC, USA, https://ntrs.nasa.gov/citations/19930093938 (last access: 4 April 2022), 1933.

Olsen, N. R. B. and Stokseth, S.: Three-dimensional numerical modelling of water flow in a river with large bed roughness, J. Hydraul. Res., 33, 571–581, https://doi.org/10.1080/00221689509498662, 1995.

Palmer, M. A., Hondula, K. L., and Koch, B. J.: Ecological restoration of streams and rivers: shifting strategies and shifting goals, Annu. Rev. Ecol. Evol. S., 45, 247–269, https://doi.org/10.1146/annurev-ecolsys-120213-091935, 2014.

Perkins, W. A. and Richmond, M. C.: MASS2, modular aquatic simulation system in two dimensions, theory and numerical methods, Tech. Rep., Pacific Northwest National Laboratory (PNNL), Richland, WA (United States), https://doi.org/10.2172/919712, 2007.

Podhorányi, M., Unucka, J., Bobál', P., Říhová, V., Podhoranyi, M., Unucka, J., Bobal, P., and Rihova, V.: Effects of LIDAR DEM resolution in hydrodynamic modelling: model sensitivity for cross-sections, Int. J. Digit. Earth, 6, 3–27, https://doi.org/10.1080/17538947.2011.596578, 2013.

Potter, C., Zhang, P., Klooster, S., Genovese, V., Shekhar, S., and Kumar, V.: Understanding controls on historical river discharge in the world's largest drainage basins, Earth Interact., 8, 1–21, https://doi.org/10.1175/1087-3562(2004)008<0001:UCOHRD>2.0.CO;2, 2004.

Powell, D. M.: Flow resistance in gravel-bed rivers: progress in research, Earth-Sci. Rev., 136, 301–338, https://doi.org/10.1016/j.earscirev.2014.06.001, 2014.

Richards, K. S.: Simulation of flow geometry in a riffle-pool stream, Earth Surface Processes, 3, 345–354, https://doi.org/10.1002/esp.3290030403, 1978.

Richmond, M. C. and Perkins, W. A.: Efficient calculation of dewatered and entrapped areas using hydrodynamic modeling and GIS, Environ. Modell. Softw., 24, 1447–1456, https://doi.org/10.1016/j.envsoft.2009.06.001, 2009.

Richmond, M. C., Perkins, W. A., and Chien, Y.: Regional scale simulation of water temperature and dissolved gas variations in the Columbia River basin, in: HydroVision 2002 Technical Papers, June, HCI Publications, Portland, OR, USA, https://www.researchgate.net/publication/278848235 (last access: 4 April 2022), 2002.

Rickenmann, D. and Recking, A.: Evaluation of flow resistance in gravel-bed rivers through a large field data set, Water Resour. Res., 47, W07538, https://doi.org/10.1029/2010WR009793, 2011.

Rodriguez, J. F., Bombardelli, F. A., García, M. H., Frothingham, K. M., Rhoads, B. L., and Abad, J. D.: High-resolution numerical simulation of flow through a highly sinuous river reach, Water Resour. Manag., 18, 177–199, https://doi.org/10.1023/B:WARM.0000043137.52125.a0, 2004.

Schlichting, H.: Boundary layer theory, 7th edn., McGraw-Hill Publishing, New York, ISBN13 9780070553347, ISBN10 0070553343, 1979.

Sinha, S., Liu, X., and Garcia, M. H.: A three-dimensional water quality model of Chicago Area Waterway System (CAWS), Environ. Model. Assess., 18, 567–592, https://doi.org/10.1007/s10666-013-9367-1, 2013.

Sinha, S. K., Sotiropoulos, F., and Odgaard, A. J.: Three-dimensional numerical model for flow through natural rivers, J. Hydraul. Eng., 124, 13–24, https://doi.org/10.1061/(ASCE)0733-9429(1998)124:1(13), 1998.

Smith, M. W.: Roughness in the earth sciences, Earth-Sci. Rev., 136, 202–225, https://doi.org/10.1016/j.earscirev.2014.05.016, 2014.

Sun, T., Meakin, P., Jøssang, T., and Schwarz, K.: A simulation model for meandering rivers, Water Resour. Res., 32, 2937–2954, https://doi.org/10.1029/96WR00998, 1996.

Talbot, T. and Lapointe, M.: Numerical modeling of gravel bed river response to meander straightening: The coupling between the evolution of bed pavement and long profile, Water Resour. Res., 38, 1074, https://doi.org/10.1029/2001WR000330, 2002.

Thompson, D. M., Nelson, J. M., and Wohl, E. E.: Interactions between pool geometry and hydraulics, Water Resour. Res., 34, 3673–3681, https://doi.org/10.1029/1998WR900004, 1998.

Tonina, D. and Buffington, J. M.: Hyporheic exchange in gravel bed rivers with pool-riffle morphology: Laboratory experiments and three-dimensional modeling, Water Resour. Res., 43, W01421, https://doi.org/10.1029/2005WR004328, 2007.

Tonina, D., McKean, J. A., Benjankar, R. M., Wright, C. W., Goode, J. R., Chen, Q., Reeder, W. J., Carmichael, R. A., and Edmondson, M. R.: Mapping river bathymetries: evaluating topobathymetric LiDAR survey, Earth Surf. Proc. Land., 44, 507–520, https://doi.org/10.1002/esp.4513, 2019.

Tsai, W.-P., Feng, D., Pan, M., Beck, H., Lawson, K., Yang, Y., Liu, J., and Shen, C.: From calibration to parameter learning: Harnessing the scaling effects of big data in geoscientific modeling, Nat. Commun., 12, 5988, https://doi.org/10.1038/s41467-021-26107-z, 2021.

USACE: Hydraulics design of flood control channels, US Army Corps of Engineers Engineer Manual, pp. 1–183, https://apps.dtic.mil/sti/pdfs/ADA402524.pdf (last access: 4 April 2022), 1994.

van Niekerk, A., Vogel, K. R., Slingerland, R. L., and Bridge, J. S.: Routing of heterogeneous sediments over movable bed: model development, J. Hydraul. Eng., 118, 246–262, https://doi.org/10.1061/(ASCE)0733-9429(1992)118:2(246), 1992.

Veldkamp, T. I., Zhao, F., Ward, P. J., De Moel, H., Aerts, J. C., Schmied, H. M., Portmann, F. T., Masaki, Y., Pokhrel, Y., Liu, X., Satoh, Y., Gerten, D., Gosling, S. N., Zaherpour, J., and Wada, Y.: Human impact parameterizations in global hydrological models improve estimates of monthly discharges and hydrological extremes: A multi-model validation study, Environ. Res. Lett., 13, 055008, https://doi.org/10.1088/1748-9326/aab96f, 2018.

Versteeg, H. K. and Malalasekera, W.: An introduction to computational fluid dynamics: the finite volume method, 2nd edn., Pearson Eduction Limited, England, ISBN-13 9780131274983, 2007.

Wampler, P. J.: Rivers and streams – water and sediment in motion, Nature Education Knowledge, 3, 18, https://www.nature.com/scitable/knowledge/library/rivers-and-streams-water-and-26405398/ (last access: 4 April 2022), 2012.

Wei, X., Cai, S., Ni, P., and Zhan, W.: Impacts of climate change and human activities on the water discharge and sediment load of the Pearl River, southern China, Scientific Reports, 10, 16743, https://doi.org/10.1038/s41598-020-73939-8, 2020.

Wilcox, D. C.: Turbulence modeling for CFD, 3rd edn., DCW Industries, La Canada, Calif, ISBN-10 1928729088, ISBN-13 978-1928729082, 2006.

Wilson, C., Yagci, O., Rauch, H. P., and Olsen, N.: 3D numerical modelling of a willow vegetated river/floodplain system, J. Hydrol., 327, 13–21, https://doi.org/10.1016/j.jhydrol.2005.11.027, 2006.

Wohl, E., Angermeier, P. L., Bledsoe, B., Kondolf, G. M., MacDonnell, L., Merritt, D. M., Palmer, M. A., Poff, N. L. R., and Tarboton, D.: River restoration, Water Resour. Res., 41, W10301, https://doi.org/10.1029/2005WR003985, 2005.

Wohl, E., Lane, S. N., and Wilcox, A. C.: The science and practice of river restoration, Water Resour. Res., 51, 5974–5997, https://doi.org/10.1002/2014WR016874, 2015.

Wood, E. F., Roundy, J. K., Troy, T. J., van Beek, L. P. H., Bierkens, M. F. P., Blyth, E., de Roo, A., Döll, P., Ek, M., Famiglietti, J., Gochis, D., van de Giesen, N., Houser, P., Jaffé, P. R., Kollet, S., Lehner, B., Lettenmaier, D. P., Peters-Lidard, C., Sivapalan, M., Sheffield, J., Wade, A., and Whitehead, P.: Hyperresolution global land surface modeling: Meeting a grand challenge for monitoring Earth's terrestrial water, Water Resour. Res., 47, W05301, https://doi.org/10.1029/2010WR010090, 2011.

Xu, D., Ivanov, V. Y., Li, X., and Troy, T. J.: Peak runoff timing is linked to global warming trajectories, Earth's Future, 9, e2021EF002083, https://doi.org/10.1029/2021EF002083, 2021.

Yang, Y., Pan, M., Lin, P., Beck, H. E., Zeng, Z., Yamazaki, D., David, C. H., Lu, H., Yang, K., Hong, Y., and Wood, E. F.: Global Reach-Level 3-Hourly River Flood Reanalysis (1980–2019), B. Am. Meteorol. Soc., 102, E2086–E2105, https://doi.org/10.1175/BAMS-D-20-0057.1, 2021.

Zalesak, S. T.: Fully multidimensional flux-corrected transport algorithms for fluids, J. Comput. Phys., 31, 335–362, https://doi.org/10.1016/0021-9991(79)90051-2, 1979.

Zhou, T., Bao, J., Huang, M., Hou, Z., Arntzen, E., Song, X., Harding, S. F., Titzler, P. S., Ren, H., Murray, C. J., Perkins, W. A., Chen, X., Stegen, J. C., Hammond, G. E., Thorne, P. D., and Zachara, J. M.: Riverbed hydrologic exchange dynamics in a large regulated river reach, Water Resour. Res., 54, 2715–2730, https://doi.org/10.1002/2017WR020508, 2018.